Timing and Petrogenesis of the Permo-Carboniferous Larvik Plutonic Complex, Oslo Rift, Norway : New Insights from U-Pb, Lu-Hf, and O Isotopes in Zircon

Ramo, O. Tapani

2022-12-01

Ramo , O T , Andersen , T & Whitehouse , M J 2022 , ' Timing and Petrogenesis of the Permo-Carboniferous Larvik Plutonic Complex, Oslo Rift, Norway : New Insights from U-Pb, Lu-Hf, and O Isotopes in Zircon ' , Journal of Petrology , vol. 63 , no. 12 . https://doi.org/10.1093/petrology/egac116

http://hdl.handle.net/10138/353803
https://doi.org/10.1093/petrology/egac116

OXFORD

Journal of Petrology, 2022, **63**, 1–29
https://doi.org/10.1093/petrology/egac116
Original Manuscript

Timing and Petrogenesis of the Permo-Carboniferous Larvik Plutonic Complex, Oslo Rift, Norway: New Insights from U–Pb, Lu-Hf, and O Isotopes in Zircon

O Tapani Rämö [1,*], Tom Andersen[2,3] and Martin J Whitehouse[4]

[1]Department of Geosciences and Geography, Geology and Geophysics Research Program, P.O. Box 64, FI-00014 University of Helsinki, Finland
[2]Department of Geosciences, University of Oslo, present address: Natural History Museum, University of Oslo, P.O. Box 1172 Blindern, N-0318 Oslo, Norway
[3]Department of Geology, University of Johannesburg, PO Box 524, Auckland Park, 2006, Johannesburg, South Africa
[4]Swedish Museum of Natural History, Box 50 007, SE 104 05 Stockholm, Sweden

*Corresponding author. Telephone: +358504480223. E-mail: tapani.ramo@helsinki.fi

Abstract

The Permo-Carboniferous Oslo Rift is a narrow, aborted continental rift with comparatively little extension but voluminous magmatism, developed at a Proterozoic lithospheric discontinuity. On the southern flank of the onshore part of the rift, the multiple intrusive phase Larvik plutonic complex (LPC) encompasses almost the width of the rift with a conspicuous over- to undersaturated assemblage of monzonite (larvikite, tønsbergite) and nepheline syenite (lardalite, foyaite). We present new single-crystal U–Pb–, Lu–Hf–, and O–in–zircon isotope data for the intrusive centers of the complex. U–Pb ages of slightly over- to undersaturated monzonites show a shift in igneous activity from 299 Ma on the eastern edge of the complex to 289 Ma in the west. The western part of the complex is built of two consanguineous magmatic systems with a northward shift in the locus of magmatism, from 296 to 289 Ma (undersaturated monzonite) and 296 to ~288 Ma (nepheline syenite). Moreover, an early oversaturated monzonite was emplaced in the eastern part of the complex at ~302 Ma. The Hf and O isotope composition of the monzonites and nepheline syenites shows little variation with zircon ε_{Hf} (295 Ma) values of +5.5 to +8 and $\delta^{18}O$ values of +4.79‰ to +5.49‰. No change in isotope values is observed with varying alkalinity and the Hf and O isotope compositions are interpreted as mantle source values. The source of the precursors of the monzonitic and nepheline syenitic magmas was probably a mildly depleted, sublithospheric peridotite in the lithosphere-asthenosphere boundary zone (at 3–4 GPa). Rhyolite–MELTS modeling implies polybaric fractionation of weakly alkaline basaltic melts from the source having led to an oversaturated/saturated liquid line of descent at ~0.5 GPa and an undersaturated one at ~1 GPa. Magmatism had an imperative role in the evolution of the rift by localizing strain and weakening the lithosphere along the discontinuity. A fractionating crustal melt column was tapped at varying depths in the course of advancing rupturing with no significant mixing of the over- and undersaturated melts, and magma batches were emplaced as sequential nested plutons in response to differential opening of the rift. Among continental saturated-undersaturated alkaline complexes, the LPC may be unique in the emplacement of successive magma batches across a continental rift in the direction of opening, tapping of increasingly deeper parts of the melt column with advancing rifting, and intrusion of two contemporaneous, contrasting magmatic lineages at the end of igneous activity. The marked lithospheric step at the rift locus in the Precambrian basement of southeastern Norway was probably the driving force for the inception and evolution of the Larvik magmatic system.

Keywords: zircon, Oslo Rift, Norway, isotope geology, geochronology

INTRODUCTION

Continental rifts mark the sites of sublithospheric mechanical and thermal disturbances that result in thinning of the lithosphere, uplift and rupture of continental crust, and enhanced magmatism and sedimentation along rift zones, and may lead to breakup of continents and formation of new sea floor (e.g. Morgan & Baker, 1983). Volcanism associated with continental rifts spans a wide spectrum from silica-undersaturated lavas (melilitite, nephelinite, phonolite) and carbonatite through tholeiite to dacite and rhyolite, and the magmatic association varies by location (e.g. Artemieva & Meissner, 2012). For instance, the two currently active Neogene rifts, Kenya and Rio Grande, are of similar dimensions and extent but comprise substantially different volcanic traits. The Kenya rift is an alkaline igneous province with alkaline and transitional basalts, basanite and nephelinite to carbonatite, whereas the Rio Grande rift is mostly tholeiitic with subordinate more alkaline magmas (Keller *et al.*, 1991, and references therein). Overall, the composition of rift lavas reflects melt sources in the mantle, continental crust as contaminant, and time- and space-integrated evolution of the magmas (e.g. Thompson & Gibson, 1994).

The Permo-Carboniferous Oslo Rift belongs to a system of Late Paleozoic rift structures in the Skagerrak–North Sea–Norwegian–Greenland Sea region (Ziegler, 1978; Neumann *et al.*, 1992, 2004)

Received: November 2, 2021. **Revised:** October 20, 2022. **Accepted:** November 1, 2022

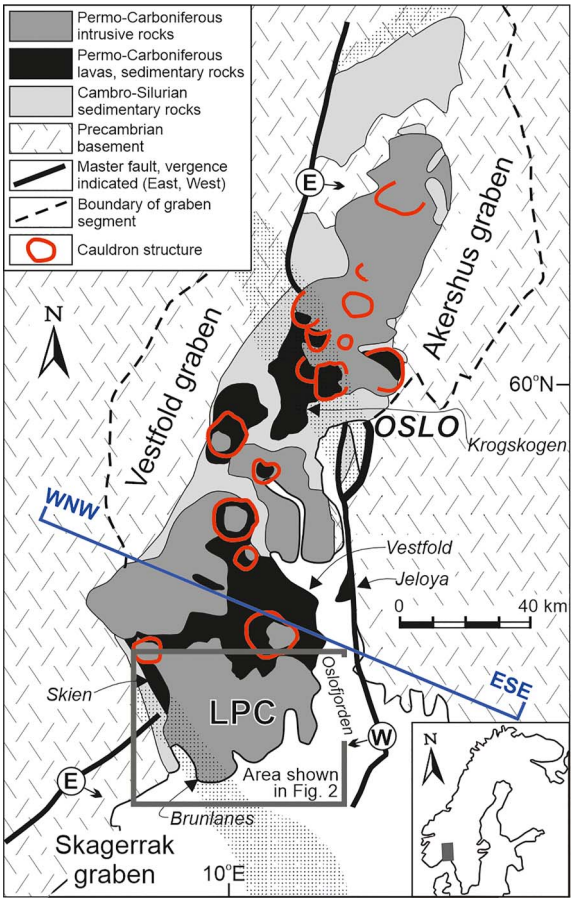

Fig. 1. Simplified geological map of the Permo-Carboniferous Oslo Rift. Three of the four half grabens of the rift are shown: Skagerrak (northern part), Vestfold, and Akershus; the Rendal graben is north of Akershus and falls outside map area. The grabens show opposite subsidence polarity with alternating east- and west-verging master faults with direction of vergence indicated (E → and W→, respectively). Stippled overlay pattern indicates accommodation zones between rift segments. Five locations with preserved early rift (B1) mafic lavas (Brunlanes, Skien, Jeløya, Vestfold, Krogskogen) are indicated; most of the Permo-Carboniferous lavas marked on the map are intermediate in composition (latitic rhomb porphyries). Cauldron structures formed in the mature stage of the rift are indicated in red. LPC marks the Larvik plutonic complex. Inset shows area of principal map relative to Fennoscandia. Position of the geological map of the Larvik plutonic complex (Fig. 2) is indicated, blue WNW-ESE line marks the position of crust–mantle transects shown in Fig. 16. Modified from Corfu & Dahlgren (2008), Larsen *et al.* (2008), and Pedersen & van der Beek (1994).

and is a typical narrow continental rift (cf. Buck, 1991). The rift was initiated within cold and stable Precambrian lithosphere, and it is characterized by a relatively low degree of extension but profuse magmatism, with an estimated total melt volume of ≥120 000 km^3 (Neumann *et al.*, 2004; Pascal *et al.*, 2004). After ~50 my of magmatic and tectonic activity, extension ceased and the rift was uplifted and now exposes a 1–3-km-deep section (Oftedahl, 1952) through the rift structure with plutonic rocks partly covered by intermediate and basic lavas and other rift-fill successions (Fig. 1). Seismic studies indicate that a lithospheric step between two Precambrian lithospheric domains with contrasting thickness existed prior to the formation of the rift (Babuška *et al.*, 1988; Kinck *et al.*, 1993; Plomerová *et al.*, 2001).

The southern on-shore part of the Oslo Rift is dominated by the Larvik plutonic complex (LPC), which encompasses almost the full width of the rift (Fig. 1). The bulk of the intrusive rocks of the LPC are weakly silica over- to undersaturated monzonites (larvikites), whereas intrusions in the northwestern part of the complex are nepheline syenites (lardalites, foyaites; e.g. Barth, 1945). These intrusive rocks are considered high-level expressions of deeper magmatic systems with a mantle-derived mafic precursor (Neumann, 1980; Neumann *et al.*, 1986), and they are compositionally comparable to latite (rhomb porphyry) lavas, which partly cover the plutonic rocks of the rift (Fig. 1).

The current understanding of the emplacement history and petrogenesis of the LPC is largely based on elemental geochemical and whole-rock Sr, Nd, and Pb isotope data, the latter only on the monzonites (Neumann, 1980; Neumann *et al.*, 1988; Rasmussen *et al.*, 1988; Sundvoll *et al.*, 1990). A small number of zircon and baddeleyite U–Pb ages (Dahlgren *et al.*,1996, 1998) are in the 299–292-Ma range and indicate an older intrusive age than suggested by an earlier overall Rb-Sr isochron age of 277 ± 3 Ma (Rasmussen *et al.*, 1988). The U–Pb data also imply that the internal intrusive history of the LPC may be resolvable by single-zircon U–Pb data.

In applying isotope fingerprinting to model plutonic systems, concomitant Hf and O isotope data from individual zircon grains dated using the U–Pb method have proven to be an efficient tool to decipher internal variations in complex plutonic systems (e.g. Heinonen *et al.*, 2015; Barnes *et al.*, 2021). Such methods have not, however, been applied to the LPC. On the other hand, the LPC is one of the first plutonic complexes for which a polybaric crystallization history from a mantle-derived parent was successfully documented (Neumann, 1980). In the absence of energy-conserved modeling tools at that time, Neumann (1980) based her arguments mainly on analogy with experimental results in relatively simple systems.

In continental rift settings, nepheline syenites characterized by leucocratic alkali feldspar and nepheline-dominated assemblages are found as relatively shallow, subvolcanic complexes and are often associated with silica-saturated plutonic rocks (e.g. Platt, 1996). Individual complexes that include both silica-saturated or -oversaturated (OS) and silica-undersaturated (US) assemblages are comparatively rare, however. In the Mesoproterozoic Gardar rift of South Greenland, the Ilímaussaq complex contains both OS and US syenites with an US augite syenite emplaced first, followed by quartz syenite and alkali granite and finally an agpaitic fractionation assemblage (pulaskite, foyaite, and kakortokite) (Upton *et al.*, 2003; Upton, 2013). In the Kangerlussuaq complex of the Tertiary Province of East Greenland, the bulk of the intrusion consists of quartz syenite with minor pulaskite and foyaite in the central part of the igneous body (Riishuus *et al.*, 2006, 2008). The Mesozoic Chilwa complex of Malawi comprises a US sequence of overlapping pulaskitic-foyaitic intrusive centers, which show concomitant decrease in age and the level of undersaturation and are associated with an OS syenite–granite intrusion (Woolley & Platt, 1986). Regarding the origin of OS–US complexes, closed-system processes driven either by mantle melting (Ashwal *et al.*, 2016) or by polybaric fractionation of a primary magma (e.g. Le Masurier *et al.*, 2003) and open-system processes involving crustal contamination combined with fractional crystallization (Foland *et al.*, 1993; Wilson *et al.*, 1995; Riishuus *et al.*, 2008) have been invoked.

The LPC is a rare example of a continental rift-associated, multiple intrusive phase alkaline complex with a conspicuous OS–US rock assemblage. In order to provide further insight into the origin and evolution of intraplate OS–US associations, we have separated zircon grains from all the intrusive centers of the LPC and analyzed them for their U–Pb, Lu–Hf, and O isotope composition. We use the results to refine the temporal evolution

and emplacement sequence of the intrusive segments of the LPC and present a refined polybaric evolution model based on energy-conserved modeling for the OS–US rocks of the LPC. We also discuss the identity of the mantle source of the LPC and the significance of OS–US magmatism in the early opening of the Oslo Rift as well as the role of pre-existing lithologic structure in promoting mantle melting and generation of a mildly alkaline mafic parental melt for the LPC.

GEOLOGIC SETTING

The Oslo rift

The Oslo Rift comprises a 400-km-long and 60–120-km-wide zone of half grabens with down-faulted blocks of Phanerozoic sedimentary rocks, lavas, and intrusions (Larsen *et al.*, 2008). The southernmost segment of the rift is the submerged Skagerrak graben, followed to the north by the Vestfold, Akerhus, and Rendal grabens (Fig. 1). These polarity offset grabens have east-or west-verging major faults that alternate in sequence and are separated by 10–20-km-wide accommodation zones (Sundvoll & Larsen, 1994; Neumann *et al.*, 2004; Larsen *et al.*, 2008). The Oslo Rift transects the Paleo- to Neoproterozoic lithosphere of the Southwest Scandinavian Domain of the Fennoscandian Shield, with crust formation mainly at 1.75–1.55 Ga and tectonometamorphic overprinting and granitic magmatism in the late Mesoproterozoic (Andersen *et al.*, 2001, 2004; Neumann *et al.*, 2004; Bingen *et al.*, 2008; Larsen *et al.*, 2008). The rift opened in response to dextral movement along the WNW-striking Sorgenfrei–Tornqvist zone, which meets the Skagerrak graben in northwestern Denmark (Ro & Faleide, 1992). Some of the major faults of the rift overlap with Precambrian deformation zones and show evidence of brittle deformation overprinting older, ductile deformation structures (Brøgger, 1886; Swensson, 1990; Sundvoll & Larsen, 1994; Pascal *et al.*, 2004; Ebbing *et al.*, 2005; Gabrielsen *et al.*, 2017). The rift is characterized by a pronounced gravity high with residual anomalies peaking ~25 mGal at the transition of the Vestfold and Akerhus grabens (Ramberg, 1976; Wessel & Husebye, 1987; Pedersen & van der Beek, 1994).

Early alkaline mafic volcanism in the Oslo Rift occurred between the Vestfold and Skagerrak grabens (Brunlanes, Skien; Figs 1 and 2) at 300.4 ± 0.7 to 298.9 ± 0.7 Ma (Corfu & Dahlgren, 2008; see also Segalstad, 1979). Comparable early volcanic units (termed B1 basalts by Oftedahl, 1952) are found in the eastern part of the Vestfold graben (Jeløya, Vestfold; Neumann *et al.*, 2002, 2004) and between the Vestfold and Akerhus grabens (Krogskogen; Ramberg & Larsen, 1978). According to Larsen *et al.* (2008), the early volcanism was followed by eruption of the rhomb porphyry lavas and emplacement of their plutonic counterparts, slightly over- to undersaturated monzonites (larvikites) and nepheline syenites (lardalite, foyaite). This magmatism probably spanned most of the duration of rift evolution, as shown by recent U–Pb ages on lavas and intrusions from the Krokskogen area (Corfu & Larsen, 2020; see also Pedersen *et al.*, 1995, and Dahlgren *et al.*, 1996). The bulk of the rhomb porphyry and larvikite magmatism was followed by formation of central volcanoes and calderas, graben fill clastic sedimentation, and emplacement of syenitic to granitic batholiths north of the LPC (Larsen *et al.*, 2008). Small, compositionally transitional mafic intrusions are also found (Neumann *et al.*, 1985).

Magmatism in the Oslo Rift lasted several tens of my. Rb–Sr whole-rock isotope data by Sundvoll *et al.* (1990) imply a duration of ~60 my and onset of rift magmatism at ~300 Ma. Subsequent U–Pb zircon geochronology indicates, in general, slightly older magmatic ages and a possibly somewhat narrower time window (on the order of 50 my) (Corfu & Dahlgren, 2008; Olsen, 2018; Corfu & Larsen, 2020).

The Larvik plutonic complex

The LPC occupies the southernmost exposed part of the Oslo Rift (Lutro & Nordgulen, 2008; Figs. 1 and 2). The prevalent rock type is *larvikite* (Brøgger, 1890; Table 1), currently defined as augite syenite or monzonite with rhomb-shaped ternary feldspar, locally with distinctive schiller (Le Maitre *et al.*, 2002). Further rock types include *tønsbergite* (red, quartz-bearing larvikite), *lardalite* (nepheline syenite with ternary feldspar), and other nepheline syenites (e.g. *foyaite*, *hedrumite*; Table 1) as well as miaskitic to agpaitic alkaline pegmatites. The LPC also shows small concordant magnetite clinopyroxenite (jacupirangite s.l.) bodies hosted by larvikite (Bergstøl, 1972; Andersen & Seiersten, 1994).

Based on curvilinear, stepped topographic lineaments, orientational fabrics (alignment of rhomb-shaped feldspars, igneous lamination and layering), 4–50-m-wide fine-grained contact variants conforming to the curvilinear structures, comb textures, and arc-shaped magnetic anomalies, Petersen (1978) proposed that the complex is a sequence of intrusive centers (plutonic counterparts of volcanic centers across the rift) with unilateral younging to the west. The ten intrusive centers of Petersen (1978) are marked in Fig. 2 (ring segments 1–10; in the following, Rings 1–10). Each of them has been suggested to represent emplacement of (at least) one batch of intermediate magma, which underwent at least some in situ fractionation (Neumann, 1980). The westward younging direction of the intrusive centers proposed by Petersen (1978) was confirmed by TIMS U–Pb zircon/baddeleyite ages reported by Dahlgren *et al.* (1996, 1998): 298.6 ± 1.4 Ma for Ring 2 and 292.1 ± 0.8 Ma for Ring 9.

The ring segments show systematic modal variation. Rings 1 and 2 comprise tønsbergite and quartz bearing larvikite, larvikite in Rings 3 and 5 is devoid of quartz and nepheline, and larvikite of Rings 4 and 6 through 8 is nepheline bearing (Barth, 1945; Raade, 1973; Oftedahl & Petersen, 1978). Rings 9 and 10 are dominated by nepheline syenites (lardalite, foyaite); a nepheline syenite intrusion is also found in the western part of Ring 6 (Groome, 2017). In Ring 10, an intrusive relationship is found between lardalite (older) and foyaite (younger) (Oftedahl & Petersen, 1978), the latter also intruding the northern parts of Ring 5 (Fig. 2).

SAMPLES EXAMINED

We have analyzed zircon from 24 samples retrieved from the G. Raade and W.C. Brøgger collections of the Natural History Museum, University of Oslo. The samples (Table 2, Fig. 2) cover the whole LPC from Ring 1 to 10 and the compositional range of the main plutonic rock types of the complex from quartz-bearing tønsbergite to nepheline syenite (cf. Brøgger, 1933; Raade, 1973; Petersen, 1978; Neumann, 1980). One sample (Bo; tønsbergite) was taken from Ring 1 in the Bolærne archipelago along the northwestern fringe of the oldest intrusive center of Petersen (1978). For Ring 2, two tønsbergites (Hu, 637) come from the eastern flank and two larvikites (490, 498) from the western segment of the ring structure. Three larvikites were analyzed from Ring 3, one (622) from the south and two (502, 503) from the north. Ring 4 was sampled at two locations, close to the contact with Ring 5 (2; nepheline-bearing larvikite southwest of Sandefjord) and Ring 6 (367; nepheline-bearing larvikite northeast of Brunlanes). For Ring 5, one sample (457; larvikite) comes from the central part of

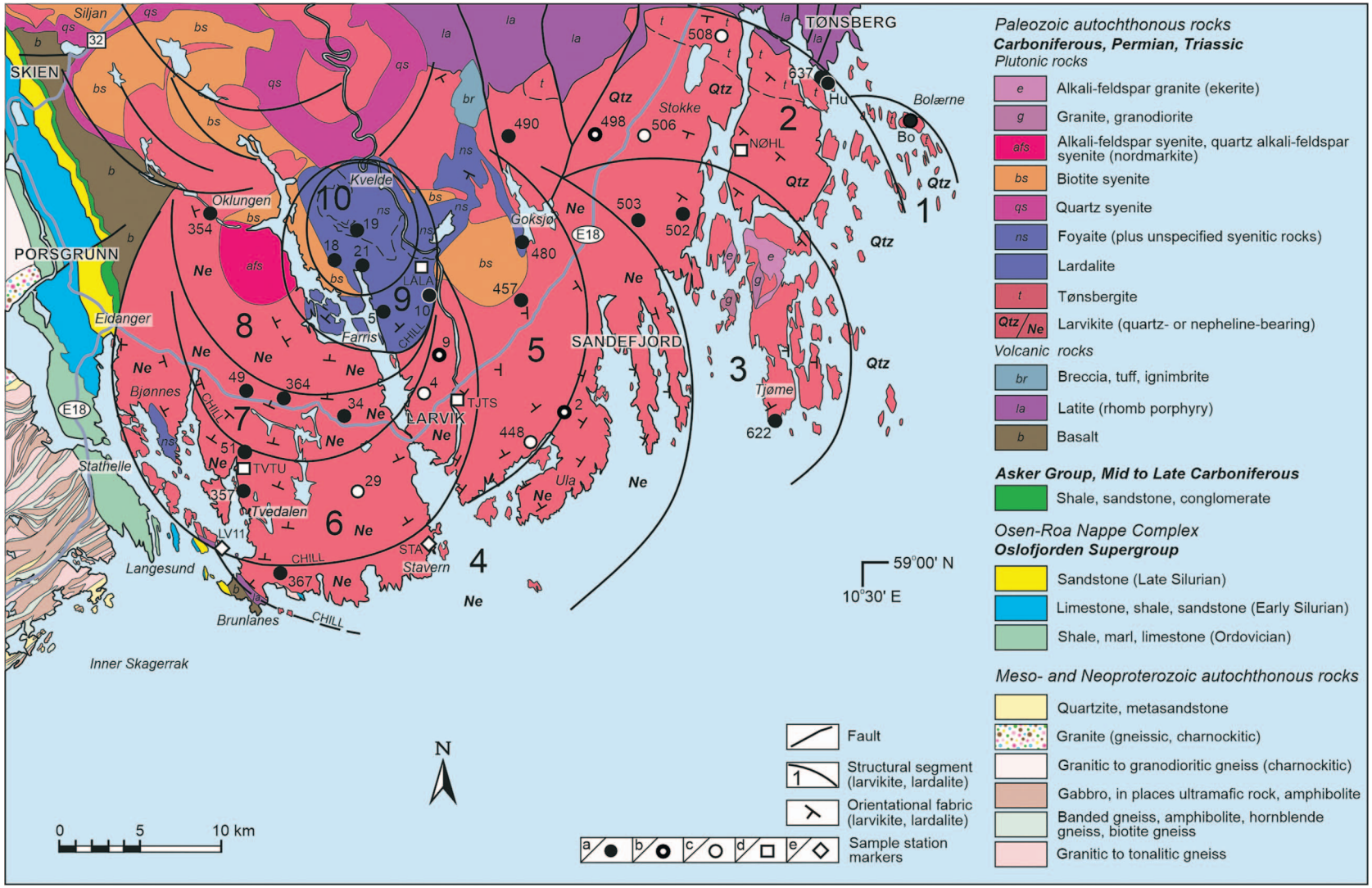

Fig. 2. Geological map of the Larvik plutonic complex, based on the current geological map of the Oslo Region (Lutro & Nordgulen, 2008). Ring fracture segments (1–8 larvikite, tønsbergite; 9–10 lardalite, foyaite), orientational fabrics (alignment of rhomb-shaped feldspar megacrysts, igneous lamination) in larvikite and lardalite, and chill zones observed at margins of intrusive centers are from Petersen (1978). Dashed line through ring structures 9 and 10 marks the boundary between lardalite and foyaite (Oftedahl & Petersen, 1978), the dashed lines in the northern part of ring structure 2 show the southern extent of tønsbergite (Raade, 1973). For larvikite, ring structures with modal quartz (Qtz) and nepheline (Ne) are indicated, with two of the structures (3, 5) showing neither quartz nor nepheline (cf. Petersen, 1978). Location of samples is mostly in reference to the Natural History Museum, University of Oslo archives used in this study (W.C. Brøgger and G. Raade collections). Key to sample stations: a, this study; b, this study and Neumann (1980); c, Neumann (1980); d, Dahlgren *et al.* (1998); e, pegmatite samples (cf. Andersen *et al.*, 2019). Principal roads across the map area are indicated. Modified from Lutro & Nordgulen (2008), Oftedahl & Petersen (1978), Raade (1973), and Groome (2017).

Table 1: Local rock names of the LPC and the Greater Oslo Rift

Rock type	Characterization	Reference
Ditroite	Granular nepheline syenite, biotite bearing with cancrinite and primary calcite	Brøgger (1890)
Ekerite	Peralkaline granite, anorthoclase micropertite and small amounts of alkali amphibole and alkalipyroxene	Brøgger (1906)
Foyaite	Hypersolvus nepheline syenite, trachytic texture caused by platy alkali feldspar	Le Maitre *et al.* (2002)
Hedrumite	Porphyritic alkali feldspar syenite, trachytic texture with biotite and minor alkali amphibole, alkali pyroxene, and nepheline in groundmass	Brøgger (1898)
Jacupirangite	Alkali pyroxenite, Ti-augite with minor T-magnetite, nepheline, apatite, perovskite, and melanite	Derby (1891)
Kjelsåsite	Plagioclase-rich larvikite, variety of augite syenite or monzonite with alkali pyroxene, hornblende, and biotite	Brøgger (1933)
Lardalite	Coarse-grained nepheline syenite, rhomb-shaped alkali, or ternary feldspar and large nepheline	Brøgger (1890)
Larvikite	Augite syenite or monzonite, rhomb-shaped ternary feldspar (with schiller), barkevikite, Ti-augite, and lepidomelane; minor nepheline, quartz, and olivine may be present	Brøgger (1890)
Mænaite	Hypabyssal albite-bearing altered trachyte	Brøgger (1898)
Nordmarkite	Quartz-bearing alkali feldspar syenite, microperthite with minor biotite, alkali amphibole or alkali pyroxene	Brøgger (1890)
Pulaskite	Alkali feldspar syenite, nepheline bearing with varying amouts of alkali pyroxene, alkali amphibole, fayalite, and biotite	Derby (1891)
Tønsbergite	Red variety of larvikite, alkali feldspar syenite with rhomb-shaped feldspar	Brøgger (1898)

the structure and another one (480) from a foyaite that intrudes larvikite by Lake Goksjø. Three nepheline-bearing larvikites were taken from Ring 6: 9 from the northeastern part of the structure north of Larvik and 51 and 357 from the southern part by the Tvedalen larvikite quarry area (cf. Dahlgren, 2010). Three nepheline-bearing larvikites (34, 49, 364) come from the central part of Ring 7 and one (354) from the western part of Ring 8. Two lardalites (5, 10) were taken from Ring 9 and two lardalites (18, 21) and one foyaite (19) from Ring 10.

Petrography

The petrography of the samples is summarized in Table 2. As is common in felsic alkaline rocks, larvikite, lardalite, and foyaite feldspar crystallized before the mafic silicates. The feldspar is in general a single *ternary feldspar* exsolved to variable degree; in varieties with iridescence, growth of exsolution lamellae stopped at the submicroscopic stage and other varieties have mesoperthite in which the potassic phase is generally quite heavily sericitized. Albite is found as overgrowths and interstitial fillings, and in one of the samples (354), also as an alteration product along feldspar grain boundaries. Feldspar in tønsbergite is stained red by fine-grained hematite. In larvikite, *nepheline* (where present) is a minor phase, found interstitially and as irregular inclusions or exsolutions (Widenfalk, 1972) in feldspar. In lardalite and foyaite, nepheline is present as inclusions in feldspar and as a major interstitial mineral and the state of preservation varies from good to extensively replaced by fine-grained, high-birefringence material (natrolite, sericite). *Sodalite* is an interstitial phase in one of the two foyaite samples studied. In the silica-oversaturated larvikite and tønsbergite, primary *quartz* is found as an interstitial mineral, in tønsbergite also in replacement products after clinopyroxene (with hematite).

The main mafic minerals are olivine, clinopyroxene, biotite, amphibole, and Fe–Ti oxides. *Olivine* is restricted to lardalite and the silica-undersaturated varieties of larvikite and is heavily altered to silicate-iron oxide intergrowths (iddingsite) or chlorite. In some samples, olivine is rimmed by clinopyroxene. *Clinopyroxene* is the most common interstitial mineral in larvikite and lardalite. It is generally quite pale and only weakly pleochroic. In the classification of Morimoto *et al.* (1989), clinopyroxene compositions reported by Neumann (1976) are diopside with $Fe/(Mg+Fe) \leq 0.25$ in lardalite and 0.25–0.45 in larvikite. In foyaite, and one of the lardalite samples (10), pyroxene is zoned with pale cores and green, pleochroic rims or overgrowths, with up to 80% of aegirine component (Neumann, 1976). *Amphibole* is less common and forms interstitial grains intergrown with clinopyroxene. It is pleochroic, yellowish-brown to olive or dark brown. Amphibole compositions reported by Neumann (1976) are magnesio-hastingsite to richterite by the classification of Leake *et al.* (1997). *Biotite* is strongly pleochroic, brownish-yellow to dark brown. It was crystallized in two generations, as a primary magmatic interstitial mineral and as ubiquitous reaction rims between magnetite and feldspar. *Chlorite* is found in a few samples as an alteration product of olivine. *Apatite* and *zircon* are abundant accessory minerals in all the samples studied, *titanite* and *baddeleyite* are found in some samples.

ANALYTICAL METHODS

Heavy mineral separation

The samples used in this study were ~750-g splits of coarse crushed material previously used for radiometry by Raade (1973). Approximately 25 g of this coarsely crushed material of each sample was sieved to 50-mesh. The fine fraction was rinsed under water to remove dust and dried on filtration paper at 40°C. Light minerals (feldspars, nepheline, quartz) were removed by heavy liquid separation using LST Fastfloat sodium heteropolytungstate (2.80 ± 0.02 g/cm^3; Central Chemical Consulting Pty Ltd). The heavy fraction was collected on filtration paper, washed with distilled water, and dried. Magnetite was removed with a neodymium hand magnet. A low to intermediate magnetic susceptibility heavy fraction (zircon ± baddeleyite, apatite, and titanite) was recovered using the FRANTZ isodynamic magnetic separator. Individual crystals were hand picked from this fraction under a binocular microscope and mounted in epoxy disks for single crystal laser ablation multicollector inductively coupled plasma mass spectrometry (LA-MC-ICP/MS) and secondary ion mass spectrometry (SIMS) analysis. The zircons were polished and examined using back-scattered electron and cathodoluminescence imaging

Table 2: Summary of isotope data on the LPC

Sample no.	Rock type	Petrography(*	^{206}Pb–^{238}U age (Ma)(**	ε_{Hf} value (295 Ma)(***	$\delta^{18}O_{V\text{-}SMOW}$ (‰)(§
Ring 1					
Bo	Tønsbergite	Perthitic feldspar, stained brick red by hematite dust; interstitial quartz; interstitial mafic silicate minerals largely replaced by quartz-hematite pseudomorphs	298.7 ± 0.4 / 1.18 / 60	6.5 ± 0.3 / 1.1 / 49	
Ring 2					
490	Larvikite	Pervasively sericitized feldspar; quartz, amphibole, biotite interstitial	295.3 ± 1.4 / 2.6 / 24	7.4 ± 0.3 / 0.8 / 28	
498	Larvikite	One feldspar, sericitized; clinopyroxene interstitial; little quartz	296.7 ± 0.7 / 2.4 / 41	7.5 ± 0.3 / 1.2 / 51	5.21 ± 0.11 / 1.3 / 17
637	Tønsbergite	One stained feldspar; quartz, zoned clinopyroxene interstitial, replaced by quartz + hematite	308 ± 4 / 11 / 20	6.5 ± 0.4 / 0.8 / 21	4.97 ± 0.19 / 1.4 / 8
Hu	Tønsbergite	See sample 637	303.1 ± 1.6 / 2.8 / 17	6.3 ± 0.4 / 0.7 / 21	
Ring 3					
502	Larvikite	One feldspar; olivine relics, magnetite with biotite coronas	292 ± 3 / 13 / 29	7.5 ± 0.3 / 1.5 / 49	
503	Larvikite	One feldspar; interstitial clinopyroxene, biotite, apatite, magnetite	296.8 ± 0.7 / 3.2 / 41	7.3 ± 0.3 / 1.1 / 53	5.03 ± 0.27 / 6.5 / 14
622	Larvikite	One exolved feldspar; pseudomorphic olivine, interstitial biotite magnetite, apatite	301.4 ± 1.1 / 0.69 / 13	8.0 ± 1.0 / 0.1 / 3	
Ring 4					
2	Larvikite	One feldspar; nepheline enclosed by feldspar; interstitial clinopyroxene, biotite, magnetite	296.1 ± 0.6 / 2.0 / 39	6.9 ± 0.3 / 1.0 / 42	
367	Larvikite	One exolved feldspar; clinopyroxene, biotite interstitial; pseudomorphs after nepheline, fine-grained, recrystallized bands	295.5 ± 0.9 / 1.3 / 42	7.7 ± 0.3 / 1.3 / 36	5.35 ± 0.22 / 4.6 / 14
Ring 5					
457	Larvikite	One feldspar; clinopyroxene, biotite, apatite, magnetite interstitial	296.4 ± 0.7 / 1.15 / 40	7.3 ± 0.3 / 1.5 / 39	
480	Foyaite	One feldspar, albite overgrowths; interstitial nepheline; green pyroxene, amphibole, biotite, titanite	288.5 ± 0.8 / 1.16 / 55	5.4 ± 0.3 / 1.1 / 27	5.10 ± 0.34 / 3.3 / 6
Ring 6					
9	Larvikite	One feldspar; nepheline enclosed in feldspar and interstices; interstitial clinopyroxene, biotite, magnetite, apatite	292.8 ± 0.8 / 1.16 / 46	5.7 ± 0.4 / 2.0 / 41	5.34 ± 0.18 / 2.7 / 13
51	Larvikite	One feldspar; nepheline in feldspar and interstices; interstitial olivine rimmed by clinopyroxene, biotite, magnetite	293.0 ± 1.3 / 1.3 / 24	7.2 ± 0.5 / 2.1 / 23	4.97 ± 0.18 / 1.8 / 9
357	Larvikite	One feldspar; nepheline in feldspar and interstices; interstitial olivine and clinopyroxene, biotite, magnetite, apatite	295.7 ± 0.9 / 1.11 / 30	6.6 ± 0.4 / 1.1 / 27	5.09 ± 0.12 / 1.5 / 16
Ring 7					
34	Larvikite	One feldspar, partly exolved; nepheline interstitial and enclosed by feldspar, heavily altered; interstitial olivine (altered), clinopyroxene, amphibole, biotite, magnetite	n.a.(§§	n.a.(§§§	
49	Larvikite	One feldspar, partly exolved; altered nepheline; intersitial olivine rimmed by clinopyroxene, biotite	295 ± 2 / 1.7 / 13	7.1 ± 0.4 / 1.1 / 15	
364	Larvikite (altered)	One feldspar; nepheline, replaced by natrolite; olivine, replaced by chlorite	292.4 ± 1.0 / 1.03 / 20	5.8 ± 0.8 / 1.0 / 5	n.a.(#
Ring 8					
354	Larvikite (altered)	Perthitic alkali feldspar, with albite replacement along grain boundaries, interstitial albite; pseudomorphs after nepheline; calcite fracture fillings	288.6 ± 1.3 / 1.6 / 20	5.9 ± 0.6 / 2.2 / 22	4.79 ± 0.10 / 1.13 / 13
Ring 9					
5	Lardalite	One feldspar; fresh interstitial nepheline; clinopyroxene and olivine	293.4 ± 0.9 / 6.4 / 46	6.1 ± 0.3 / 1.8 / 51	5.49 ± 0.18 / 2.9 / 14
10	Lardalite	One feldspar; nepheline inclusionsin feldspar and interstices; clinopyroxene (colorless and pale green), biotitte, magnetite, apatite	296.3 ± 0.9 / 1.06 / 44	6.7 ± 0.3 / 0.8 / 42	5.36 ± 0.09 / 0.4 / 16

(Continued)

Table 2: Continued

Sample no.	Rock type	Petrography(*	^{206}Pb–^{238}U age (Ma)(**	ε_{Hf} value (295 Ma)(***	$\delta^{18}O_{V\text{-}SMOW}$ (‰)(§
Ring 10					
18	Lardalite	One feldspar; interstitial nepheline; interstitial clinopyroxene, olivine, magnetite, biotite	289.0 ± 0.6 / 1.08 / 56	6.2 ± 0.3 / 1.4 / 38	5.40 ± 0.10 / 1.2 / 17
21	Lardalite	One feldspar; nepheline in feldspar and interstices; clinopyroxene, olivine, magnetite, biotite	289.8 ± 0.8 / 1.6 / 41	6.5 ± 0.4 / 2.3 / 43	
19	Foyaite	One feldspar; interstitial (altered) nepheline, sodalite; green clinopyroxene; olivine, biotite, titanite, apatite	287.0 ± 1.2 / 1.9 / 26	6.6 ± 0.6 / 3.3 / 32	

Note: Samples Bo (Bolærne) and Hu (Husøy) from the W.C. Brøgger collection, numbered samples from the G. Raade collection of the Oslo Mineralogical-Geological Museum
*For more detailed petrography of the samples, see Raade (1973) and Neumann (1980)
**Weighted mean ages (with 2SD error, MSWD value, and number of spots averaged indicated) of the data shown in Supplementary File 1.1
***Weighted mean values (with variation at 2 SD, MSWD value, and number of spots averaged indicated) of the data shown in Supplementary File 2.1 Initial ε_{Hf} calculated using $\lambda = 1.867 * 10^{-11}$ y^{-1} and chondritic values of $^{176}Hf/^{177}Hf = 0.282785$ and $^{176}Lu/^{177}Hf = 0.0336$
§Weighted mean values (with variation at 2 SD, MSWD value, and number of spots averaged indicated) of the data shown in Supplementary File 3.
§§Three spots measured, one formally concordant spot only (^{206}Pb–^{238}U age of 347 ± 3 Ma; Supplementary File 1.1)
§§§No spots measured #Mount included titanite only

in a SEM to identify zoning and locate inclusions and structural defects.

U–Pb and Lu–Hf isotope geochemistry (LA-MC-ICP/MS)

The single crystal U–Pb and Lu–Hf isotope analyses were performed using a Nu Plasma HR multicollector ICPMS with a U–Pb collector block, the first, major batch of zircons (2009–2010) with a New Wave/Merchantek LUV-213 Nd:YAG laser microprobe and zircons analyzed for oxygen isotopes (2017) with a CETAC 213 nm laser, both at the Department of Geosciences, University of Oslo, Norway. Ablations were made in helium, which was mixed with argon prior to entering the ICP. U–Pb and Lu–Hf analyses were made mostly on the same zircon grain or zone within a grain, the Lu–Hf spots positioned at U–Pb spots analyzed earlier.

For the U–Pb analyses, the laser beam diameter was 40-μm beam, repetition rate was 10 Hz, and energy density ≤ 0.10 J/cm^2. Ablations were static, and measurements were made in time-resolved mode. Time-resolved ablation traces of homogeneous reference sampes showed that $^{206}Pb/^{238}U$ and $^{207}Pb/^{235}U$ ratios did not change over time, suggesting that laser-induced fractionation of the U/Pb ratio (e.g. Košler, 2008) was negligible at the instrumental conditions used. The contribution of ^{204}Hg from the plasma was eliminated by on-mass background measurement prior to each analysis. At the low laser power used, no excess ionization of Hg during ablations was observed, giving a constant counting rate of ≤1000 cps at mass number 204. The baseline for common lead was established during each analytical session from the counting rate at mass 204 for well-characterized, common lead-free refrence zircons (91 500, GJ-1). ^{235}U was calculated from the signal at mass 238 using a natural $^{238}U/^{235}U = 137.88$. Zircons used for calibration were GJ-01 (600.8 ± 0.4 Ma; Schaltegger *et al.*, 2015), 91 500 (1065 Ma; Wiedenbeck *et al.*, 1995), in the 2017 sessions also A382 (1877 ± 2 Ma, Huhma *et al.*, 2012). The protocols used for data reduction follow Andersen *et al.* (2009) and Rosa *et al.* (2009). 'Matrix effects' encountered in LA-ICP/MS U–Pb analysis comprise laser-induced fractionation of elemental ratios, processes in the sample introduction system, and mass discrimination in the plasma source (Jackson *et al.*, 2004, and references therein). Different strategies for compensation have been proposed; in this study, we have followed the approach of Jackson *et al.* (2004), in which homogeneous segments of the time-resolved ablation traces of the unknown zircons are integrated and matched with the corresponding time-segments on the standards used for calibration. Common lead was monitored on mass 204, which also has a contribution from ^{204}Hg in the plasma gas. Where the signal on mass 204 from an unknown did not exceed that of the average of the common lead-free reference zircons used for calibration, common lead was considered to be less than the detection limit, and no correction was applied. No grains with detectable common lead were used for age calculation. IsoplotEx 3.0 (Ludwig, 2003) was used to plot and calculate the U–Pb ages with decay constants of Jaffey *et al.* (1971). Formally concordant spots (127 of 169 spots) measured for the Plešovice reference zircon in 2009–2010 define a weighted mean ^{206}Pb–^{238}U age of 337.7 ± 0.7 (2σ) Ma (Supplementary File 1.1). This is in good agreement with the corresponding ID-TIMS age of Plešovice zircon, 337.1 ± 0.4 Ma (Sláma *et al.*, 2008). For the 2017 analyses, an in-house reference zircon STA from a pegmatite in the LPC gave a weighted mean ^{206}Pb–^{238}U age of 294.4 ± 1.7 Ma (2σ, n = 15; SD 2.1). This matches well with the ID-TIMS value of STA, 294.3 ± 0.3 Ma (L.E. Augland, pers. comm. in Andersen *et al.*, 2019).

For the Lu–Hf analyses, the laser beam diameter was 55 μm (aperture imaging mode), pulse frequency was 5 Hz, and beam energy density was ~2 J/cm^2 (static ablation). Each ablation was preceded by a 30-s on-mass background measurement. The total Hf signal obtained was in the 1.5–3.0-V range. Under these conditions, 120–150 s of ablation were required to obtain an internal precision of ≤ ±0·000020 (1SE). Isotope ratios were calculated using the Nu Plasma time-resolved analysis software. The protocol for correction of isobaric interference on mass 176 is described in Elburg *et al.* (2013). Mud Tank and Temora-2 zircons (Woodhead & Hergt, 2005) were run at frequent intervals as unknowns, with present-day $^{176}Hf/^{177}Hf$ of 0.282507 ± 48 (2σ; n = 226) and 0.282677 ± 52 (2σ; n = 92), respectively. These values are compatible with the published $^{176}Hf/^{177}Hf$ ratios of the zircons: 0.282507 ± 0.000006 (Mud Tank) and 0.282686 ± 0.000008 (Temora-2) (Woodhead & Hergt, 2005). The observed external reproducibility on the Mud Tank reference material gave a 2σ-uncertainty estimate of ±1.7 ε-units on single spot analysis. In all calculations, the ^{176}Lu decay constant of 1.867×10^{-11} a^{-1} (Scherer *et al.*, 2001, 2007; Söderlund *et al.*, 2004) and present-day chondritic

composition of $^{176}Hf/^{177}Hf = 0.282785$ and $^{176}Lu/^{177}Hf = 0.0336$ (Bouvier *et al.*, 2008) were used. The depleted mantle model of Griffin *et al.* (2000) was modified to agree with the CHUR parameters and decay constant used. Analyses with $^{178}Hf/^{177}Hf$ outside of the interval 1.46728 ± 0.00013 were rejected.

Oxygen isotope geochemistry (SIMS)

Oxygen isotopes were measured in 2016 on a second batch of zircons that were freshly mounted and polished for the purpose. After SIMS analysis, the gold coating was removed by gentle polishing with diamond paste. LA-ICPMS U–Pb spots were placed on top of the SIMS spots (visible on the sample surface), and Lu–Hf spots on top of these again, using a wider and more powerful laser beam. The oxygen isotope data were acquired using the CAMECA IMS1280 multicollector-equipped ion microprobe at the NORDSIM facility, Swedish Museum of Natural History, Stockholm, Sweden. The basic instrument setup and analytical procedure closely followed those described by Heinonen *et al.* (2015). The analyses were performed with an ~2-nA Cs^+ primary ion beam together with a normal incidence, low-energy, electron gun for charge compensation, medium field magnification (~80×) and two Faraday detectors, with the secondary ions filtered at a common mass resolution of ~2500 (M/ΔM). The measurements were carried out in pre-programmed chain-analysis mode with automatic field aperture and entrance slit centering on the ^{16}O signal. The magnetic field was locked using nuclear magnetic resonance regulation for the duration of analytical session. Each data-acquisition run commenced with a 20 μm × 20 μm pre-sputter to remove the Au layer from the analysis spot site, followed by centering steps and 64 s of data integration performed using a rastered, ~10-μm spot. Field aperture centering values were well within those for which no bias has been observed while testing standard mounts (Whitehouse & Nemchin, 2009). In the measurement chain, sets of six to seven unknowns were each bracketed by two analyses of the Geostandards 91 500 zircon. All data were normalized to measurements of the Geostandards 91 500 zircon, assuming a $\delta^{18}O$ V-SMOW value of +9.86‰ (relative to standard mean ocean water, V-SMOW) as determined by laser fluorination (Wiedenbeck *et al.*, 2004). Minor linear drift corrections (> 1 ppm/run) were applied to the data sets where applicable based on minimizing the external error on the standards. External reproducibility of ±0.17–0.21‰ (1 SD), based on standard measurements, was propagated onto the overall uncertainty for each analysis. Analyses of Temora-2 zircon during the same analytical session yielded an average of 7.99 ± 0.17‰ (1 SD, $n = 12$, 1 reject), which is within the expected value of 8.2‰ (Black *et al.*, 2004).

Modeling of liquid lines of descent

Energy-conserved model calculations of fractional crystallization trends were made using a pre-compiled Ubuntu–Linux release 1.0.2 of Rhyolite–MELTS (Gualda *et al.*, 2012, downloaded from http://melts.ofm-research.org/index.html), running in the Linux Subsystem for Windows on a Windows 10 PC system. Results were post-processed using the MELTS_Excel-Combine_tbl_1.xlsm template from Gualda & Ghiorso (2015). CIPW norms and other petrochemical parameters were calculated with GCDKit versions 4 and 6 (Janoušek *et al.*, 2006, 2016).

RESULTS

U–Pb geochronology

In total, 1077 spots on zircon crystals from 24 samples from the LPC were measured for the U–Pb isotope composition. The zircons analyzed were, in general, pristine fragments of larger prismatic or embayed crystals showing faint magmatic zonation, some fractures, and few inclusions (Fig. 3). Zircon in the OS and US rock types of the LPC is always interstitial and intergrown with mafic silicates and other late-crystallizing phases, with no indication of early (xenocrystic or antecrystic) cores. For zircon grains from any one sample, between 15 and 65 spots were measured, from one to a few points on each individual grain. All analyses that were concordant within error were used for age calculation (823 of the 1077 spots total). The ages are reported as weighted mean ^{206}Pb–^{238}U ages; this is preferred for Phanerozoic zircon for which ^{206}Pb–^{238}U is comparatively insensitive to common lead and carries practically all salient chronometric information (Ludwig, 1998).

The U–Pb isotope data on the 24 samples are listed in Supplementary File 1.1. Weighted mean ^{206}Pb–^{238}U ages were

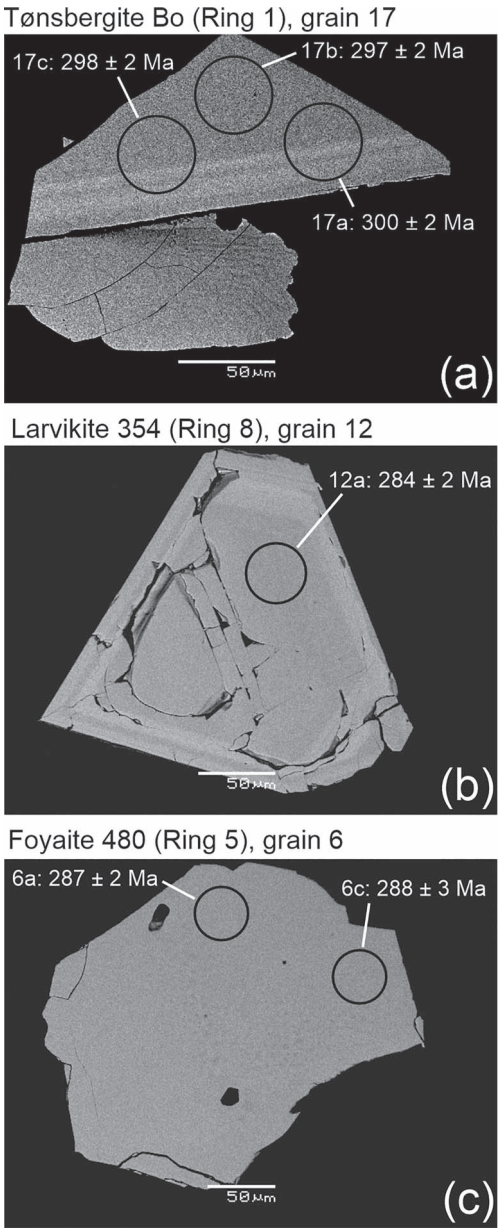

Fig. 3. Back-scattered electron images of representative zircon grains from tønsbergite in Ring 1 (a), larvikite in Ring 8 (b), and foyaite in Ring 5 (c) of the Larvik plutonic complex. U–Pb spot positions are marked and respective ^{206}Pb–^{238}U ages (with 1σ error) of the spots are shown (cf. Supplementary File 1.1).

calculated for 23 samples and are shown as individual panels in Supplementary File 1.2 and are summarized in Table 2. The ages are based on 13 (larvikites 622 from Ring 3 and 49 from Ring 7) to 60 (tønsbergite Bo from Ring 1) formally concordant analyses. The U–Pb data from individual samples range from uniform (e.g. lardalite 18 from Ring 10) to scattering beyond analytical error (e.g. tønsbergite 637 from Ring 2). The 2σ errors of the weighted mean ^{206}Pb–^{238}U ages range from ±0.42 to ±4.1 Ma (mean value ±1.2 Ma) and are considered to represent the uncertainty of the crystallization age of any one sample (Supplementary File 1.2; Table 2).

Tønsbergite

Sixty-four U–Pb spots for tønsbergite Bo from Ring 1 define a concordia age of 299.0 ± 0.5 Ma with a MSWD of concordance of 1.02 (Fig. 4a) and a narrow, unimodal distribution of spot ages (Fig. 4a inset). The weighted mean ^{206}Pb–^{238}U age is 298.7 ± 0.4 Ma (MSWD, 1.18; Fig. 4b), indistinguishable from the concordia age. Twenty spots for tønsbergite 637 show a bimodal distribution of ^{206}Pb–^{238}U ages (Fig. 4c inset) and scatter along the concordia, implying an upper intercept age of 308 ± 5 Ma when forced through the origin (Fig. 4c). The bimodal distribution is also reflected by the U concentrations, the high age (>300 Ma) zircons having between ~1400 and ~7000 ppm U. At an age of 300 Ma, this indicates an accumulated alpha radiation dose of 1.5 to 7.5 × 10^{18} alpha/g, which corresponds to a degree of radiation damage from well below the percolation point (i.e. essentially crystalline) to almost completely metamict (e.g. Nasdala *et al.*, 2004). The ^{206}Pb/^{238}U ratio of these grains is, however, uncorrelated with the uranium concentration (R^2 = 0.02), showing that there is no relationship between age and degree of radiation damage (see Supplementary File 1.3). This suggests that the grains have not been disturbed by recent alteration by weathering fluids (cf. Andersen & Elburg, 2022) and that the age bimodality is real. Sample 637 gives a weighted mean ^{206}Pb–^{238}U age of 308 ± 4 Ma, with a high MSWD = 11; (Fig. 4d). The third tønsbergite analyzed (Hu from Ring 2) comes from close to sample 637 and has a weighted mean ^{206}Pb–^{238}U age of 303.1 ± 1.6 Ma (MSWD 2.8; Supplementary File 1.2; Table 2).

Larvikite

Forty-three concordant U–Pb spots on larvikite 498 from the western segment of Ring 2 scatter along concordia and imply an upper intercept age of 301 ± 3 Ma when forced through the origin (Fig. 4e). The weighted mean ^{206}Pb–^{238}U age is 296.7 ± 0.7 Ma with a relatively high MSWD (2.4), which is also reflected in the variation of the ^{206}Pb–^{238}U age spots (Fig. 4e inset). Larvikite 354 from Ring 8 (Fig. 2) has a concordia age of 289.3 ± 1.1 Ma (Fig. 4g) and a weighted mean ^{206}Pb–^{238}U age of 288.6 ± 1.3 Ma (MSWD 1.6; Fig. 4h). The concordant spot population of 354 includes two spots with ages >300 Ma, discarded from the age calculation (Fig. 4h). The weighted mean ^{206}Pb–^{238}U ages of the larvikites in Rings 2 through 5 (Table 2; Fig. 4; Supplementary File 1.2) are within the 297–295-Ma range, except for larvikite 622 from the southern segment of Ring 3 (Fig. 2), which has a weighted mean ^{206}Pb–^{238}U age of 301.4 ± 1.1 Ma (MSWD 0.69; Supplementary File 1.2). Larvikites from Rings 6 and 7 are somewhat younger, in the 296–292-Ma range, yet clearly older than Ring 8 larvikite (Table 2).

Lardalite and foyaite

Fifty-eight spots analyzed from the zircons in foyaite sample 480 (Ring 5) define a concordia age 288.8 ± 0.8 Ma (MSWD of concordance 0.38; Fig. 4i). The weighted mean ^{206}Pb–^{238}U age of 55 spots is 288.5 ± 0.8 Ma (MSWD 1.16; Fig. 4j), which is considered as the emplacement age of the foyalite body. Forty-four spots from lardalite sample 10 from Ring 9 define a concordia age of 296.1 ± 0.9 Ma (Fig. 4k) and a weighted mean ^{206}Pb–^{238}U age of 296.3 ± 0.9 Ma (MSWD 1.06; Fig. 4l). Overall, the ^{206}Pb–^{238}U ages of the lardalites of Ring 9 are older (sample 10, 296.3 ± 0.9 Ma; sample 5, 293.4 ± 0.9 Ma) than those of lardalites and foyaites of Ring 10 (sample 21, 289.8 ± 0.8 Ma; sample 18, 289.0 ± 0.6 Ma; sample 19, 287.0 ± 1.2 Ma) (Table 2; Supplementary File 1.2). Foyaite 19 from Ring 10 (287.0 ± 1.2 Ma) is coeval within the analytical error with foyaite 480 (288.5 ± 0.8 Ma), which intrudes Ring 5 larvikite (Fig. 4j; Supplementary File 1.2).

Lu–Hf isotopes

We measured a total of 827 spots from zircon grains in the 23 samples for the Lu–Hf isotope composition. The data are shown in Supplementary File 2.1. Approximately 15 to 50 spots were measured for any one sample, with the exception of larvikites 364 (6 spots) and 622 (3 spots). The data were screened for acceptable ^{178}Hf/^{177}Hf ratios (see Supplementary File 2.1) and 784 of the 827 spots total were used to calculate the Hf isotope compositions of the 23 samples. The initial Hf isotope compositions are expressed as weighted mean ε_{Hf} (295 Ma) values calculated assuming ±1.7 ε-units as the external 2σ reproducibility based on the data measured on the Mud Tank reference zircon (Supplementary File 2.1). The weighted mean ε_{Hf} (295 Ma) values of the 23 samples are listed in Table 2 and shown in individual panels in Supplementary File 2.2, as are probability density plots that show the distribution of ε_{Hf} (295 Ma) values in each sample.

Tønsbergite

Sample Bo from Ring 1 has a weighted mean ε_{Hf} (295 Ma) value of +6.5 ± 0.3 (2σ; MSWD 1.1; number of spots 49) and a unimodal distribution of ε_{Hf} values of the 49 spots total with a peak at +6.4 (Fig. 5a, b). Sample 637 from Ring 2 has a weighted mean ε_{Hf} (295 Ma) of +6.5 ± 0.4 (2σ; MSWD 0.8; number of spots 21) (Fig. 5c). The probability density distribution of ε_{Hf} values peaks at +6.5 (Fig. 5d). The third analyzed tønsbergite (Hu from Ring 2) has a fairly uniform distribution of ε_{Hf} values (probability peak at +6.3) and a weighted mean ε_{Hf} (295 Ma) value of +6.3 ± 0.4 (2σ; MSWD 0.7; number of spots 21) (Table 2; Supplementary File 2.2). The three tønsbergites have identical ε_{Hf} (295 Ma) values at approx. +6.5 (Table 2), which is less radiogenic than the depleted mantle composition at 295 Ma (ε_{Hf} + 11.9).

Larvikite

Sample 498 has an ε_{Hf} (295 Ma) value of +7.5 ± 0.3 (2σ; MSWD 1.2; number of spots 51) and a unimodal distribution of ε_{Hf} (295 Ma) values with a peak at +7.5 (Fig. 5e, f). Sample 354 has an ε_{Hf} (295 Ma) value of +5.9 ± 0.6 (2σ; MSWD 2.2; number of spots 22) and a relatively unimodal distribution of ε_{Hf} (295 Ma) values with a main peak at +5.7 and two more radiogenic (+9.9, +11.3) outliers (Fig. 5g, h). Overall, the larvikites analyzed from Rings 2–8 have a relatively narrow range of ε_{Hf} (295 Ma) values from +5.7 to +8.0 (Table 2; Supplementary File 2.2). Larvikites from Rings 2–5 are almost identical in ε_{Hf} (+6.9 to +8.0, average + 7.4 ± 0.6, 2σ), those from Rings 6–8 are slightly less radiogenic and more varying (ε_{Hf} + 5.7 to +7.2.0, average + 6.4 ± 1.2, 2σ). The probability density distributions of the larvikite ε_{Hf} values are mostly unimodal (Supplementary File 2.2). Only larvikites 51 (Ring 6) and 354 (Ring 8) have statistically significant stray spots slightly off of the main distribution of the spots in the two samples (Fig. 5, Supplementary File 2.2). The external 2σ precision of the

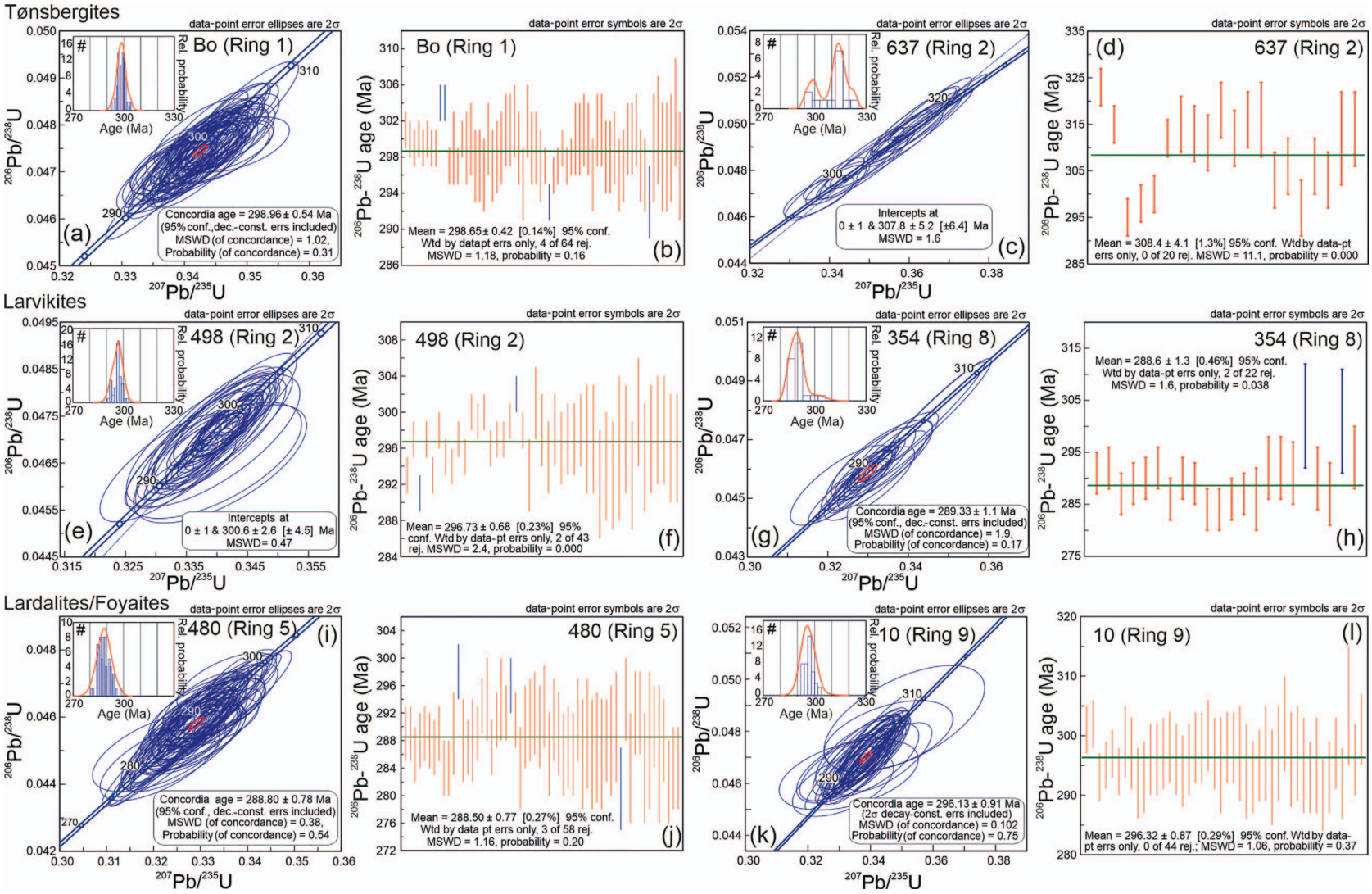

Fig. 4. U–Pb isotope data on zircon from two tønsbergites (Bo, Ring 1; 637, Ring 2), larvikites (498, Ring 2; 354, Ring 8), and lardalites/foyaites (480, Ring 5; 10, Ring 9) shown in U–Pb concordia diagrams (a, c, e, g, i, k) and weighted mean ^{206}Pb–^{238}U plots (b, d, f, h, j, l). Cumulative probability plots of the ^{206}Pb–^{238}U ages of all measured spots per sample are shown as insets in the concordia diagrams. Data points marked in blue were excluded from the calculation. U–Pb isotope data and weighted mean ^{206}Pb–^{238}U age plots of all the 23 samples are shown in Supplementary Files 1.1 and 1.2, respectively.

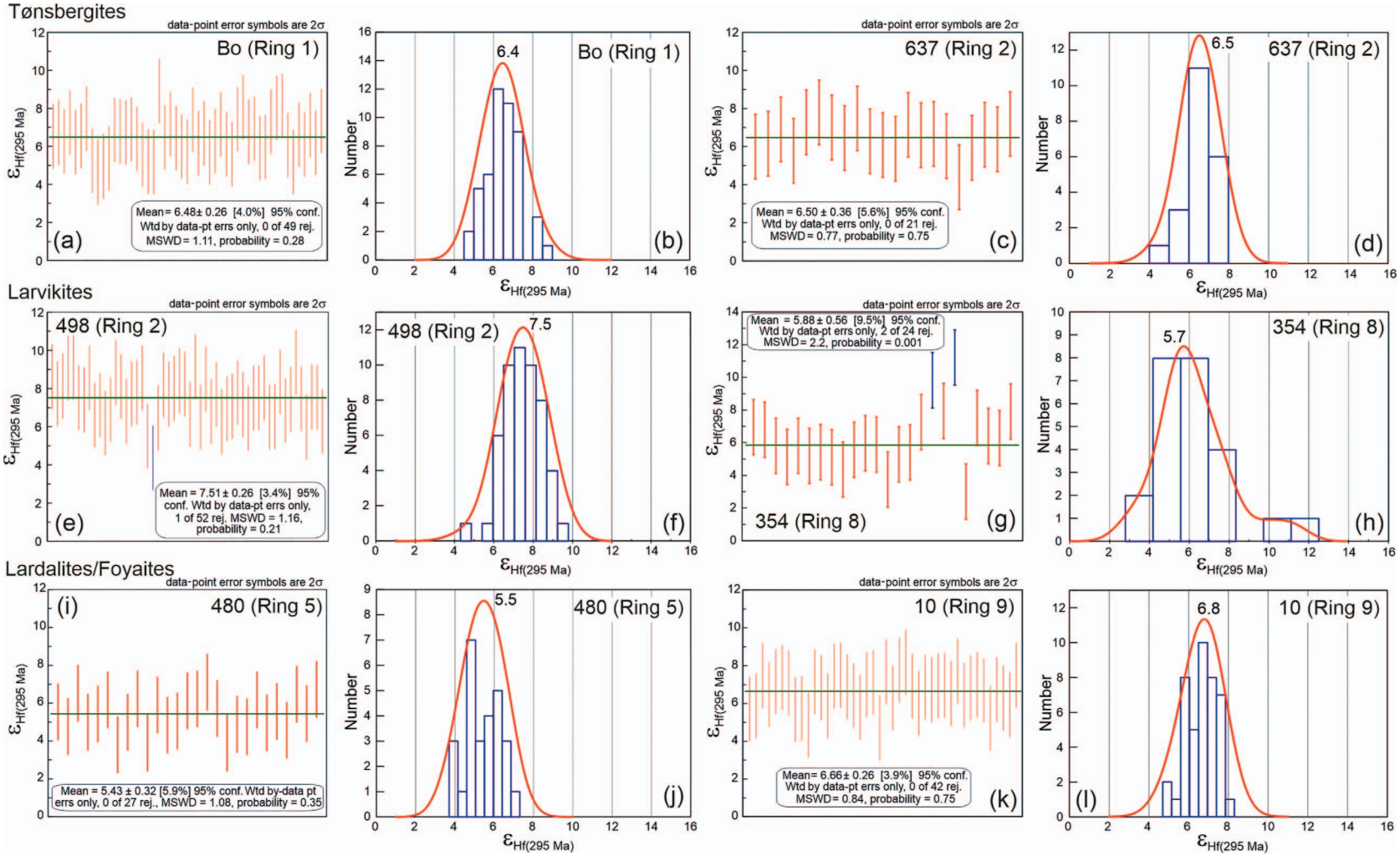

Fig. 5. Lu-Hf isotope data on zircon from two tønsbergites (Bo, Ring 1; 637, Ring 2), larvikites (498, Ring 2; 354, Ring 8), and lardalites (480, Ring 5; 10, Ring 9) shown in weighted mean ε_{Hf} (295 Ma) value (a, c, e, g, i, k) and cumulative probability plots of the ε_{Hf} (295 Ma) values (b, d, f, h, j, l). Data points marked in blue were excluded from the calculation. Lu–Hf isotope data and weighted mean ε_{Hf} (295 Ma) plots of all the 23 samples are shown in Supplementary Files 2.1 and 2.2, respectively.

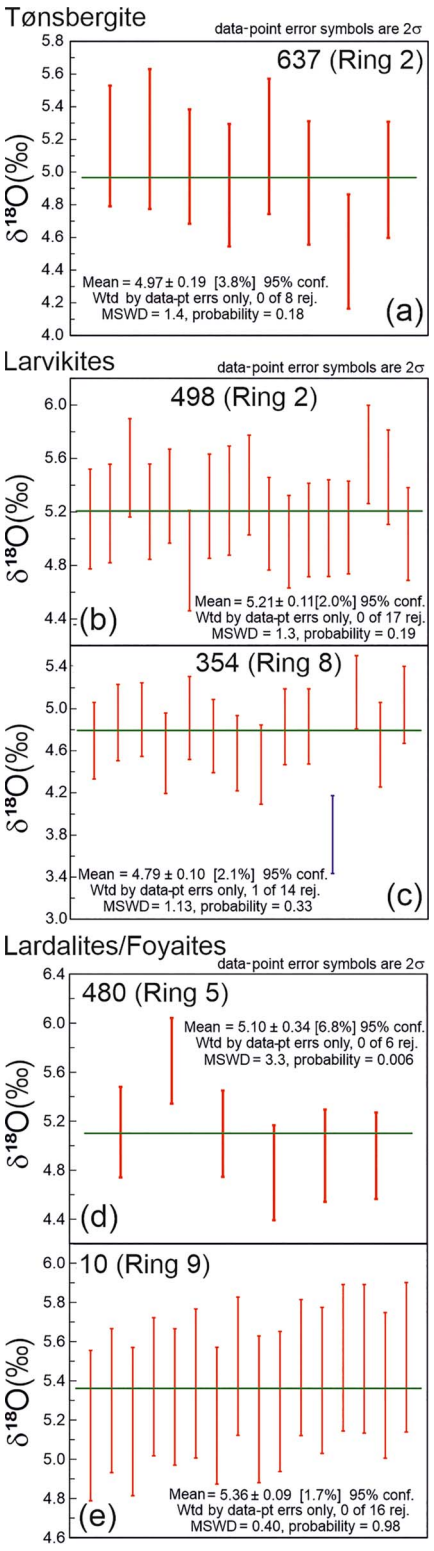

Fig. 6. Oxygen isotope data on zircon from (a) tønsbergite (637, Ring 2), (b, c) two larvikites (498, Ring 2; 354, Ring 8), and (d, e) two lardalites/foyaites (480, Ring 5; 10, Ring 9) shown as weighted mean $\delta^{18}O$ values of the measured spots. Data point marked in blue were excluded from the calculation. Oxygen isotope data and weighted mean $\delta^{18}O$ values of all the 12 samples analyzed for oxygen are shown in Supplementary Files 3.1 and 3.2, respectively.

weighted mean ε_{Hf} values is between ±0.2 and ±0.6, except for the two samples for which only a few spots are available (364 and 622, Table 2). We consider these values to be realistic estimates of the range of initial ε_{Hf} values of the samples.

Lardalite and foyaite

Foyaite sample 480 has an ε_{Hf} (295 Ma) value of +5.4 ± 0.3 (2σ; MSWD 1.1; number of spots 27) and a unimodal distribution of ε_{Hf} (295 Ma) values peaking at +5.5 (Fig. 5i, j). Lardalite 10 is more radiogenic with an ε_{Hf} (295 Ma) value of +6.7 ± 0.3 (2σ; MSWD 0.8; number of spots 42) and a unimodal distribution of ε_{Hf} values with a peak at +6.8 (Fig. 5k, l). The three other lardalites from Rings 9 and 10 (5, 18, 21) have unimodal probability density distributions and a narrow range of ε_{Hf} values (+6.1 ± 0.3, +6.2 ± 0.3, and + 6.5 ± 0.4, respectively; Table 2, Supplementary File 2.2). The lardalites of the LPC have marginally less radiogenic initial Hf isotope composition (ε_{Hf} + 6.1 to +6.7, average + 6.4 ± 0.6, 2σ) compared to the larvikites of Rings 2–5 (ε_{Hf} + 6.9 to +8.0, average + 7.4 ± 0.6, 2σ). Foyaite sample 19 from Ring 10 has a somewhat skewed distribution of ε_{Hf} values a primary probability peak at +7.0 (Supplementary File 2.2). The weighted mean value (+6.6 ± 0.6) is, however, compatible with that of the lardalites from Rings 9 and 10. The foyaite 480 from Ring 5 with ε_{Hf} of +5.4 ± 0.3 is marginally less radiogenic that the foyaite from Ring 10 and lardalites from Rings 9 and 10 and also less radiogenic than the larvikites (Table 2).

Oxygen isotopes

A total of 160 spots from zircon grains from 12 samples were measured for oxygen isotope composition, with 6–17 spots for any one sample. The data can be found in Supplementary File 3.1, weighted mean $\delta^{18}O$ value panels in Supplementary File 3.2, and summary of the results in Table 2. Oxygen isotope composition was acquired for one tønsbergite (Ring 2), seven larvikites (Rings 2–6 and 8), and four lardalites/foyaites (Rings 5 and 9–10).

Tønsbergite

Tønsbergite 637 has a weighted mean $\delta^{18}O$ value of 4.97 ± 0.19‰ (2σ; MSWD 1.4) relative to V-SMOW, based on 8 spots (Fig. 6a). This value is considered a good estimate of the oxygen isotope composition of the zircon in the tønsbergite and is at the low end of the $\delta^{18}O$ value range of zircon in melts in high-temperature equilibrium with mantle peridotite (5.3 ± 0.3‰, 1σ; Valley *et al.*, 1998).

Larvikite

Seventeen spots on larvikite 498 define a weighted mean $\delta^{18}O$ value of 5.21 ± 0.11‰ (2σ; MSWD 1.3) and 13 spots from larvikite 354 value of 4.79 ± 0.10‰ (2σ; MSWD 1.13) (Fig. 6b, c). The former is a normal value for mantle zircon, the latter implies a slightly lighter oxygen isotope composition relative to the mantle value (cf. Valley *et al.*, 1998). The five other larvikites (503, 367, 9, 51, and 357) have $\delta^{18}O$ values in the 4.97 ± 0.18‰ to 5.35 ± 0.22‰ range (Table 2; Supplementary File 3.2) and fall all within the range of normal mantle zircon. Larvikite samples from Rings 2–6 show no change in the $\delta^{18}O$ value, whereas larvikite 354 from Ring 8 has a measurably lower $\delta^{18}O$ value (Table 2; Fig. 6c).

Lardalite and foyaite

Six spots from foyaite 480 define a weighted mean $\delta^{18}O$ value of 5.10 ± 0.34‰ (2σ; MSWD 3.3; Fig. 6d), precision suffering from the small number of spots measured. Lardalite 10 has a weighted mean $\delta^{18}O$ value of 5.36 ± 0.09‰ (2σ; MSWD 0.4), based on 16 spots (Fig. 6e). The two further lardalites have $\delta^{18}O$ values of 5.49 ± 0.18‰ (5 from Ring 9) and 5.40 ± 0.10‰ (18

from Ring 10) and, together with lardalite sample 10, indicate a narrow, mantle-type range of 5.35–5.50‰ for the lardalites (Table 2; Supplementary File 3.2). The $\delta^{18}O$ value of foyaite 480, 5.10 ± 0.34‰, is compatible with this range within the experimental error. Overall, lardalites and foyaites may have marginally higher $\delta^{18}O$ values than tønsbergite and larvikites (Table 2).

DISCUSSION

Timing and emplacement sequence of the LPC

The new U–Pb zircon ages (Table 2) and pre-existing data on the LPC (Dahlgren *et al.*, 1996, 1998; STA and LV11 pegmatite zircons, Andersen *et al.*, 2019) are shown relative to the position of the samples in the ring framework of Petersen (1978) in Fig. 7a (see also Fig. 2). The profile comprises a west-southwest-directed sequence of centers (Rings 1–6) followed by a northerly trend of centers (Rings 6–10). According to Dahlgren *et al.* (1996, 1998), the emplacement of the LPC lasted 5–6 Ma (298.6 ± 1.4-Ma NØHL larvikite in Ring 2 and 292.1 ± 0.8 Ma LÅLA lardalite in Ring 9; Fig. 2). Our data refine the temporal evolution of the LPC and suggest that the emplacement pattern of the LPC was probably more complex than previously anticipated.

The spatial distribution of the U–Pb ages of the LPC are shown in a color-coded map in Fig. 8a. Samples with age errors less than ±2 Ma (25 of the 29 samples in Fig. 7a) reveal new traits in the division of crystallization ages across the LPC:

(1) Tønsbergite Hu from the northeastern flank of Ring 2 and larvikite 622 from the southern segment of Ring 3 at longitude ~10°25'E have ages just over 300 Ma, 303.1 ± 1.6 Ma, and 301.4 ± 1.1 Ma, respectively, and are corroborated by the less precise age (308 ± 4 Ma) of tønsbergite 637 from near sample HU (Fig. 2). These are marginally higher than the 298.6 ± 1.4 Ma age of NØHL larvikite in Ring 2 (Dahlgren *et al.*, 1998), and the new age, 298.7 ± 0.4 Ma of tønsbergite Bo in Ring 1 (Fig. 7a). They are also slightly higher than the U–Pb ages of the Brunlanes and Skien lavas (300.4 ± 0.7 to 298.9 ± 0.7 Ma; Corfu & Dahlgren, 2008) intruded by Rings 4 and 6 larvikites on the western flank of the LPC (Fig. 2). The ~302 Ma samples probably indicate emplacement of an oversaturated larvikite body at the outset of the opening of the Vestfold graben, not totally cannibalized by subsequent ring plutons.

(2) Four samples at latitude ~59°12'30"N (Bo, NØHL, 498, 490) show a progression of ages younging to the west (horizontal red arrow in Fig. 8a), from Ring 1 (298.7 ± 0.4 Ma; Bo) to the western part of Ring 2 (295.3 ± 1.4 Ma; 490). This implies a measurable age difference of at least 1.5 my along the traverse and a westward shift at ~1.5 cm/y of the locus of early magmatism of the LPC (Fig. 8a).

(3) The area outlined by dashed line in the middle part of the LPC (Fig. 8a) has ages that range from 296.8 to 295.3 Ma and are identical within the analytical error, averaging at 296.1 ± 1.1 Ma (2σ). This segment extends across several of the ring structures of Petersen (1978), from the western edges of Rings 2 and 3 through the border zone between Rings 4 and 5, and 4 and 6, to the south-central part of Ring 6. The emplacement of larvikites along this west-southwest-directed part of the LPC (Figs 7a and 8a) may reflect increased magma supply rate and resultant, more or less simultaneous intrusion of slightly oversaturated and undersaturated monzonitic magmas over an ~30-km-long segment in central LPC. This may also imply relatively rapid (~3 cm/y) opening of the southern part of the rift at ~296 Ma. The STA pegmatite from the southern part of the ~296-Ma segment is slightly younger, 294.3 ± 0.3 Ma, whereas the 296 ± 3 Ma age of the LV11 pegmatite north of Brunlanes (Andersen *et al.*, 2019) matches the age of the segment.

(4) From the western end of the ~296-Ma segment in the south part of Ring 6, seven larvikite samples (357, TJTS, TVTU, 9, 51, 364, 354; Fig. 2) define a northerly trend of declining ages from Ring 6 through Ring 7 to the western margin of Ring 8 (295.7 ± 0.9 to 288.6 ± 1.3 Ma; Figs. 7a, 8a). A comparable shift is recorded by the nepheline syenites (lardalite, foyaite) of Rings 9 and 10. Ring 9 is measurably older (296.3 ± 0.9 to 292.1 ± 0.8 Ma, average 294.0 Ma) than Ring 10 (289.8 ± 0.8 to 287.0 ± 1.2 Ma, average 288.6 Ma). These results reveal two concurrent magmatic lineages, one larvikitic and the other lardalitic, that built the western part of the LPC with the locus of magmatism shifting to the north with time, at ~0.25 cm/y (larvikite) to ~0.1 cm/y (lardalite, foyaite). The strongly undersaturated magmatic system shows a more restricted spatial change in the locus of magmatism with time than the slightly undersaturated system. Both larvikitic and lardalitic magmas started to feed high-level ring complexes in the western part of the LPC at ~296 Ma (Figs. 7a, 8a), and this led to the construction of the western periphery of the LPC within ~5 my or so.

(5) Magmatism in the LPC was completed by strongly undersaturated magmas, represented by foyaite 19 of Ring 10 and foyaite 480, which cuts larvikite in the northern part of Ring 5 (Fig. 2). These foyaites are coeval within analytical error (287.0 ± 1.2 vs 288.5 ± 0.8 Ma) and represent the youngest plutonic event in the LPC at ~288 Ma (Fig. 7a). The 288.6 ± 1.3 Ma larvikite (354) in the western part of Ring 8 is coeval with the foyaites, and thus monzonitic magma was available at the closure of magmatic activity of the LPC. This young LPC larvikite is ~10 my older than larvikite in the Siljan–Hvarnes ring complex that was emplaced along the northwestern margin of the LPC at ~279–277 Ma (Pedersen *et al.*, 1995; Fig. 2).

Constraints on magma sources from Sr, Nd, Hf, and O isotopes

Previously published isotope data on the LPC are available for the monzonites (tønsbergite, larvikite) only (Neumann *et al.*, 1988). $^{87}Sr/^{86}Sr$ (295 Ma) values of tønsbergite and larvikite from Rings 2, 4, 5, and 6 vary from 0.70295 to 0.70392, average at 0.7036, scatter beyond analytical error, and are less radiogenic than the Bulk Silicate Earth (BSE; Fig. 9). ε_{Nd} (295 Ma) values range from +3.7 to +4.6, average at +4.1, and are compatible within the analytical error. This is approximately half way between the depleted MORB mantle (+7.6 at 295 Ma; cf. Workman & Hart, 2005) and the chondritic composition (0). Initial whole-rock ε_{Nd} values of larvikites 498, 2, and 9 (+4.1, +4.0, +4.0; Fig. 7b) are coupled with initial zircon ε_{Hf} values (+7.7, +7.9, +6.7; Table 2) and plot on the ocean-island Nd–Hf array (not shown; cf. Salters & Hart, 1991; Johnson & Beard, 1993). These two refractory isotope systems probably provide an estimate of the isotope composition of the larvikite mantle source, which does not show the shift to unradiogenic ε_{Hf} at a given ε_{Nd} typical of the subcontinental lithospheric mantle, implying a sublithospheric (~ asthenospheric) source (cf. Griffin *et al.*, 2000).

Variation of Hf and O isotope composition in tønsbergite, larvikite, and lardalite/foyaite is shown relative to the LPC ring structures in Fig. 7b and c, respectively, and their spatial distribution is depicted in the color-coded maps of Fig. 8b and c. The ε_{Hf} (295 Ma) values are between +5.4 and + 8.0 and show relatively little variation (cf. Table 2). These initial values reflect

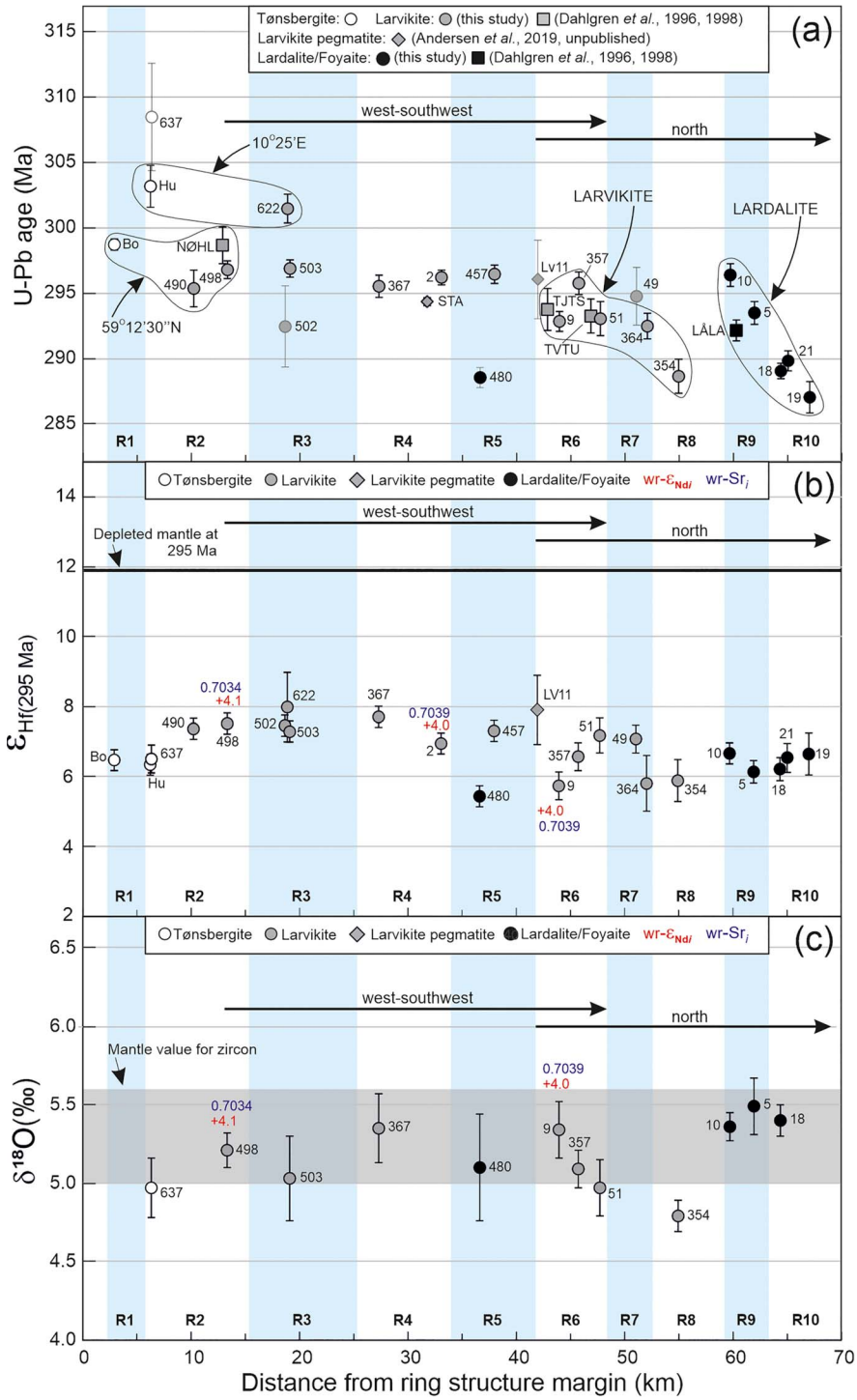

Fig. 7. Diagrams showing age and isotope composition vs spatial distribution of the analyzed samples of the Larvik plutonic complex relative to the ten ring structures (R1–R10) of Petersen (1978). The horizontal variable is distance from the outer margin of each ring structure projected toward the center of the anticipated circular structure (now obliterated by subsequent plutons of the complex, save for Ring 10 that seems to be intact; Fig. 2). (a) U–Pb age vs distance plot. U–Pb ID-TIMS zircon/baddeleyite ages for NØHL from Ring 2, TJTS and TVTU from Ring 6, and LÅLA from Ring 9 are from Dahlgren *et al.* (1996, 1998). STA is zircon from a pegmatite intruding larvikite in Ring 4 (ID-TIMS zircon age by L.E. Augland, pers. comm. in Andersen *et al.*, 2019), LV11 is zircon from pegmatite intruding basalt on the outer margin of Ring 6 (LA-ICP-MS zircon data by Andersen *et al.*, 2019). West-southwest- and north-bound sequences of the ring structures are indicated. Parallel age paths for larvikite and lardalite in the north-directed shift of the locus of magmatism are marked, as is a ~302-Ma segment in the eastern part of the Larvik complex at longitude 10°25'E, and a westward younging series of larvikites at latitude 59°12'30"N (cf. Fig. 8a). (b) Initial ε_{Hf} (295 Ma) value v distance plot. Data for the LV11 pegmatite are also shown (solution ICP-MS data analyzed by Dr J. Payne, Macquarie University, in Heinonen *et al.*, 2010) as is the ε_{Hf} (295 Ma) value of the depleted mantle (Griffin *et al.*, 2000, modified using the chondritic parameters of Bouvier *et al.*, 2008, and λ_{176} of Scherer *et al.*, 2001, 2007, and Söderlund *et al.*, 2004). (c) $\delta^{18}O$ value vs distance plot. Zircon oxygen isotope composition in normal mantle is from Valley *et al.* (1998). In (b) and (c), whole-rock initial (295 Ma) ε_{Nd} values (wr-ε_{Ndi}) and $^{87}Sr/^{86}Sr$ ratios (wr-Sr_i) of larvikites are from Neumann *et al.* (1988), the initial $^{87}Sr/^{86}Sr$ ratios recalculated using λ_{87} of $1.3972*10^{-11}$/a (Villa *et al.*, 2015). In all panels, errors of individual data points are 2σ external (cf. Table 2).

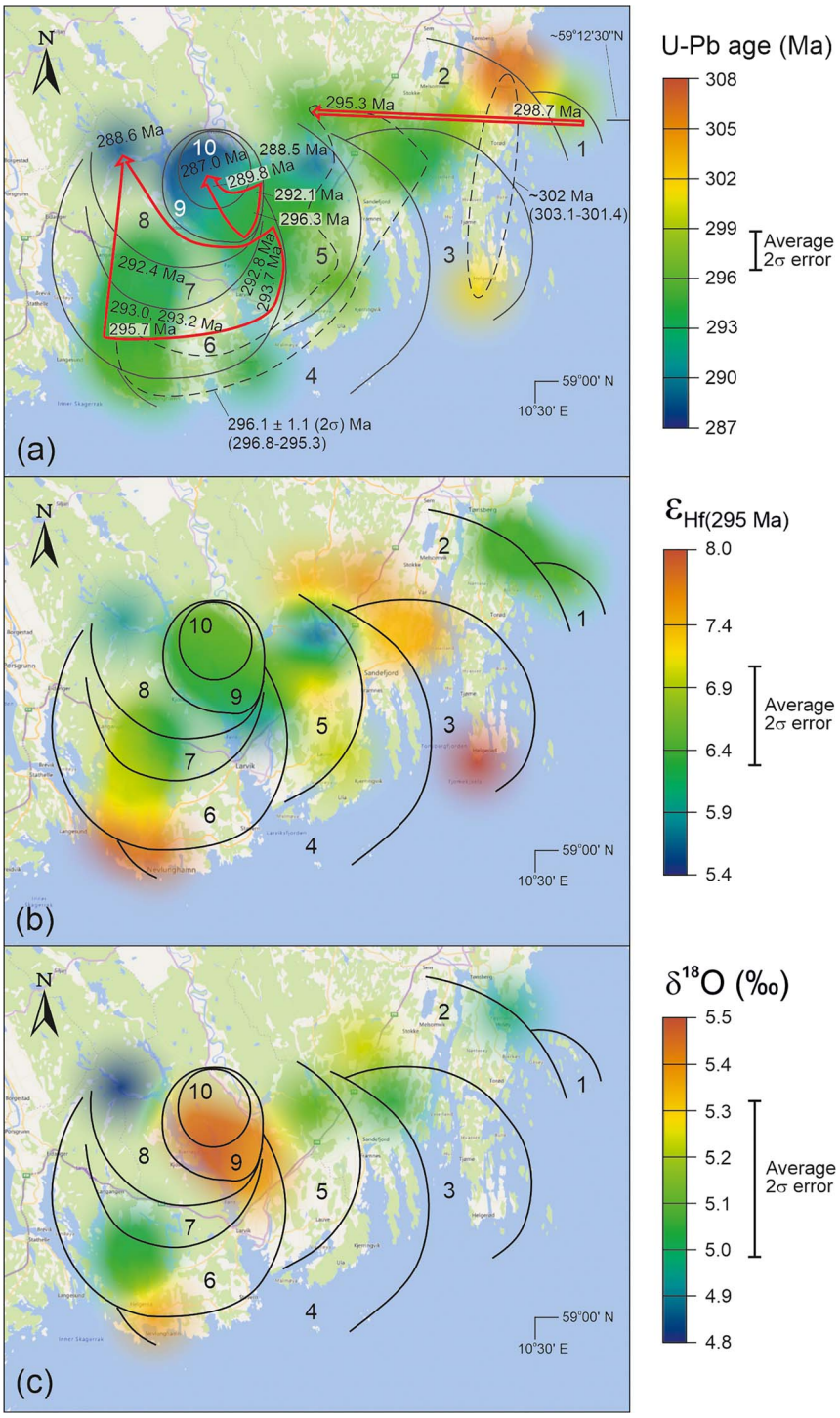

Fig. 8. Spatial distribution charts of (a) U–Pb ages, (b) ε_{Hf} (295 Ma) values, and (c) $\delta^{18}O$ values in zircon from the Larvik plutonic complex, relative to the ten ring structures of Petersen (1978) (Fig. 2; Table 2). See text for the various segments marked in (a). The charts were generated in Microsoft Excel Power View Tool (Aspin, 2016) with averaged visual aggregation of data points and maximum radius of influence. Average external 2σ errors of the three variables are indicated.

source enrichment in long-term Lu/Hf (depletion of Hf) relative to the chondritic composition but fall below the depleted mantle value at 295 Ma (+11.9). The tønsbergites of Rings 1 and 2 are slightly less radiogenic than the larvikites of Rings 2–5 and are more comparable with some of the larvikites of Rings 6–8 (Fig. 7b). The ε_{Hf} (295 Ma) values of the lardalites and foyaites in Rings 9 and 10 are between +6.1 and +6.7, and thus marginally lower than those of the larvikites in Rings 2–5 but similar to but less varying than those of the undersaturated larvikites in Rings 6–8. Foyaite 480 in Ring 5 is less radiogenic with ε_{Hf} (295 Ma) of +5.4. The zircon $\delta^{18}O$ values also span a narrow range, from +4.79‰ to +5.49‰ (Fig. 7c). This range is only slightly in excess of the average 2σ error of the $\delta^{18}O$ values (Fig. 8c) and falls in the range of normal mantle zircon, except for the youngest larvikite on the western edge of the LPC (sample 354, Ring 8). Overall, compared to larvikites, the lardalites and foyaites appear to have a bit more

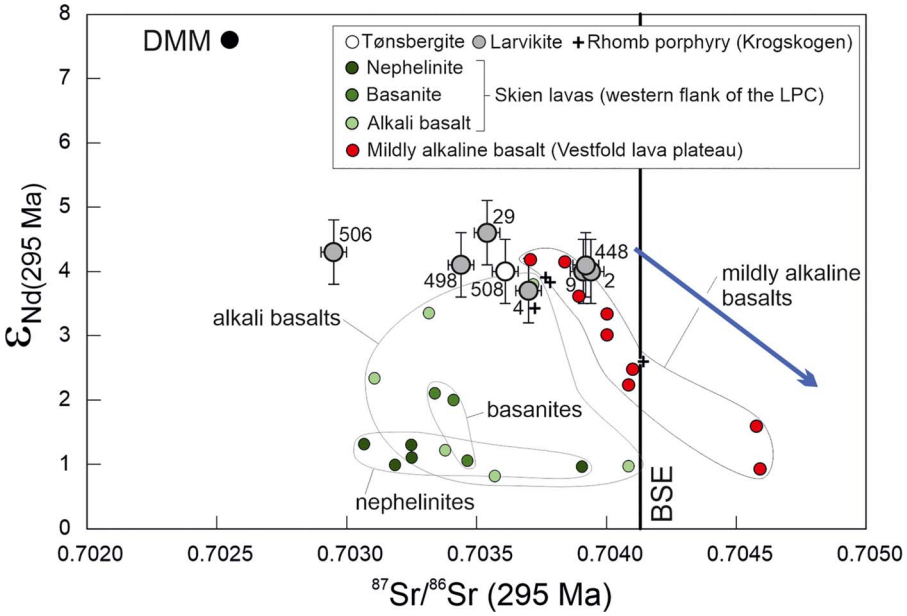

Fig. 9. Initial isotope composition of tønsbergite and seven larvikites (Neumann *et al.*, 1988) from Rings 2 and 4–6 of the Larvik plutonic complex shown in a $^{87}Sr/^{86}Sr$ vs ε_{Nd} diagram (for sample numbers, see Fig. 2). Nephelinite, basanite, and alkali basalt data from the western flank of the complex (Skien; Fig. 2) are from Neumann *et al.* (1988) and Anthony *et al.* (1989), mildly alkaline basalt data (Neumann *et al.*, 1988) from north of the complex (Vestfold; Fig. 1). Data on Krogskogen rhomb porphyries are from Neumann *et al.* (1988). Depleted MORB mantle (DMM) and Bulk Silicate Earth (BSE) are from Workman & Hart (2005). Blue arrow is crustal contamination path from Neumann *et al.* (2004). Error bars are 2σ external.

mantle-like oxygen combined with slightly less radiogenic Hf (Fig. 8b and c).

The Hf and O isotope composition of tønsbergite, larvikite, and lardalite/foyaite are shown for the older (~ 302–296 Ma) and younger (~ 296–288 Ma) segments of the LPC in Fig. 10, with the 292 ± 3 Ma larvikite (502) from the older segment (Ring 3) included in the former grouping. The older ~296 Ma group of larvikites has a well constrained initial ε_{Hf} of +7.4 ± 0.6 (2σ; Fig. 10b), whereas the younger, western larvikites are, on average, slightly less radiogenic at ε_{Hf} + 6.4 ± 1.2 (2σ; Fig. 10a). The lardalites and foyaites in Rings 9 and 10 are similar to the larvikites of the western LPC with initial ε_{Hf} of +6.4 ± 0.4 (2σ). The three tønsbergites represent early magmatism characterized by relatively unradiogenic Hf initial composition (ε_{Hf} of +6.5) and are, in this respect, similar to the western larvikites and lardalites/foyaites (Fig. 10a, b). Regarding oxygen isotopes, the older (296 Ma) larvikites have an average $\delta^{18}O$ value of +5.20 ± 0.26‰ and the one tønsbergite is marginally lighter (+4.97 ± 0.19‰) (Fig. 10d). In the western LPC, Ring 6–8 larvikites have, on average, slightly lighter oxygen than the lardalites and foyaites of Rings 9 and 10 (Fig. 10c).

Figure 11 shows the 12 samples from the LPC analyzed for both Hf and O isotopes in the $\delta^{18}O$ vs ε_{Hf} (295 Ma) space. Overall, the monzonites (larvikite, tønsbergite) from the eastern and west-central part of the LPC (Rings 2–7) and nepheline syenites (lardalite, foyaite), foyaite transecting Ring 5 larvikite, and undersaturated monzonites (larvikites) from the northeastern part of Ring 6 and from Ring 8 fall into separate fields with ε_{Hf} as the defining variable. This difference may relate to two slightly different sublithospheric mantle domains that delivered to the LPC in the course of the opening of the Oslo Rift, with the one in the west with less radiogenic Hf isotope composition.

Role of crustal contamination in OS-US suites

Cogenetic OS–US rock assemblages pose a problem as their compositions evolve toward the two thermally incompatible minima (the granite minimum and the nepheline syenite minimum) of Petrogeny's Residua System (Henderson, 1984; see also Foland *et al.*, 1993). Crustal contamination in the oversaturated melts is one mechanism that can account for the divergent trends, as demonstrated by radiogenic isotope data for the Marangudzi ring complex, Zimbabwe and the Kangerlussuaq complex, Greenland (Foland *et al.*, 1993; Riishuus *et al.*, 2008). These complexes show decreasing initial ε_{Nd} values and increasing initial $^{87}Sr/^{86}Sr$ ratios with decreasing alkalinity (shift from US to OS rock types), and can be interpreted as the result of incorporation of unradiogenic Nd and radiogenic Sr from crustal rocks to evolving (contaminating) alkaline magma. In this crustal contamination scenario, comparable shift of initial ε_{Hf} to lower values with advancing contamination is expected as continental crust is the source of unradiogenic Hf compared to the mantle (cf. Andersen *et al.*, 2002). The OS–US assemblage of the LPC is shown in an agpaitic index vs ε_{Hf} (295 Ma) plot in Fig. 12. The agpaitic index is less than one in all the samples examined (probably owing to elevated Al values in the LPC magmatic system) and no marked shift to lower ε_{Hf} values is observed with decreasing alkalinity, rather there is a hint of the opposite.

Overall, potential crustal contaminants for Oslo Rift magmatism are quite varying with initial (280 Ma) ε_{Nd} values between −15 and +10 and $^{87}Sr/^{86}Sr$ ratios between 0.705 and 0.740 (Andersen & Knudsen, 2000). The Precambrian bedrock of southern Norway also shows substantial variation in Hf isotopes: Based on data reviewed by Andersen (2014), the range of ε_{Hf} (295 Ma) values is from −35 to −5. These are remarkably different from the values in the LPC and, together with the unvarying initial Hf isotope composition of the OS–US assemblage of the complex (Fig. 12), render crustal contamination quite unlikely. Minor local contamination in the marginal parts of the complex may have occurred, however. The $\delta^{18}O$ value of larvikite 354 from Ring 8 (+4.79‰) may indicate slight contamination of larvikite magma by crustal material affected by ancient high-T exchange with seawater (cf. Valley *et al.*, 1998; Fig. 7c). Potential contaminants

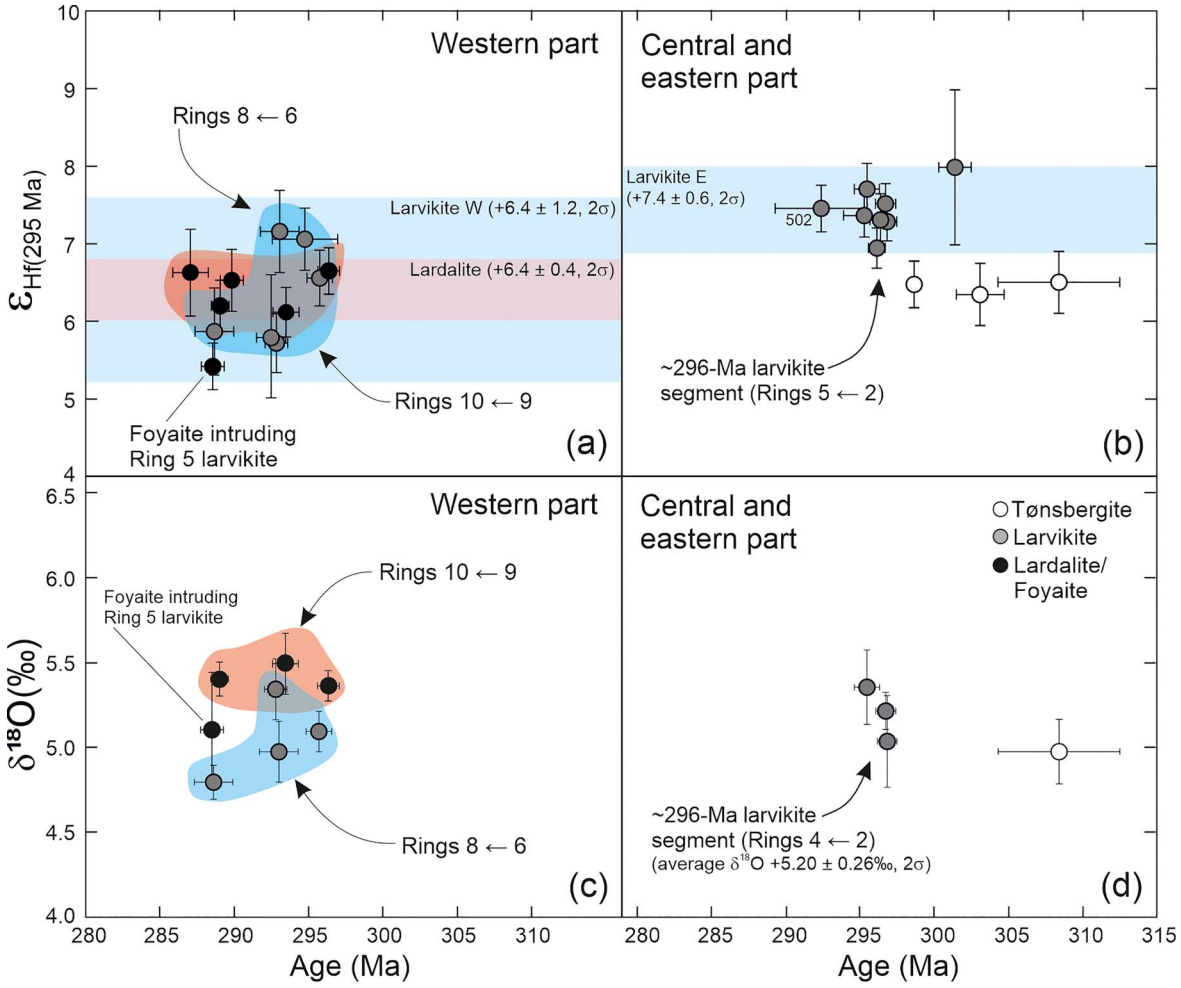

Fig. 10. Emplacement age-associated panels showing the subtle variation in the Lu–Hf-in-zircon and O-in-zircon isotope composition of the main plutonic rock types (tønsbergite, larvikite, lardalite/foyaite) of the Larvik plutonic complex (Table 2). (a) ε_{Hf} (295 Ma) values of the <296-Ma larvikites and lardalites of western LPC; (b) ε_{Hf} (295 Ma) values of the ≥296-Ma tønsbergites and larvikites of central and eastern LPC; (c) $\delta^{18}O$ values of the <296-Ma larvikites and lardalites of western LPC; (d) $\delta^{18}O$ values of the ≥296-Ma tønsbergites and larvikites of central and eastern LPC. Errors are 2σ external.

(e.g. Proterozoic gabbro, amphibolite) are exposed just west of the LPC (Fig. 2).

Liquid lines of descent in the LPC

Neumann (1980) proposed a polybaric crystallization model for the LPC with alkali to transitional basalts fractionating in a series of magma chambers at the crust–mantle boundary and up to the middle crust, involving a ternary feldspar–olivine ± clinopyroxene–Fe–Ti–oxide–apatite ± nepheline fractionate. This is compatible with the gravity high that implies presence of significant amounts of dense rocks in the lower crust/subgraben mantle underneath the Oslo Rift (Ramberg, 1976; Neumann *et al.*, 1986). In the model of Neumann (1980), the upper crust acted as density filter allowing prolonged high-P fractionation and generation of substantial amounts of intermediate residual magmas in the deep crust. Subsequently, lower-P fractionation of these weakly oversaturated and undersaturated magmas led to more strongly diverging melt compositions (larvikite, lardalite and foyaite).

Whether or not larvikites and lardalites/foyaites originated from a uniform parent magma has remained an open question (Petersen, 1978; Neumann, 1980; Dahlgren *et al.*, 1996). Our U–Pb data show that larvikite and lardalite magmas were emplaced contemporaneously in the western part of the LPC (Fig. 8a) and our Hf isotope data allow subtle differences for the mantle sources involved in generation of the parental melts for the eastern and western segments of the LPC (Figs 10 and 11). We will now examine, using the Rhyolite–MELTS approach (Gualda *et al.*, 2012), whether appropriate oversaturated/saturated and undersaturated liquid lines of descent (LLD) can be derived from mildly alkaline mafic melts in P–T–fO_2 conditions that prevailed during the early evolution of the Oslo Rift.

Modeling larvikite and lardalite liquid lines of descent

Primary magma composition and pressure regime

Within the Oslo Rift, analogs that can be considered as primary magmas in fractionation models are mafic volcanic rocks from the Skien area (Anthony *et al.*, 1989; Dunworth *et al.*, 2001) and from the Vestfold lava plateau and its eastern outlier at Jeløy Island (Schou-Jensen & Neumann, 1988; Neumann *et al.*, 1990, 2002) (cf. Fig. 1). Vestfold lavas range from picrite and ankaramite to basalt and trachybasalt, the Skien lavas are more alkaline, ranging from nephelinite through ankaramite and basanite to basalt. The Nd isotope composition of larvikites with ε_{Nd} (295 Ma) of ~ +4 (Fig. 9) shows that melts such as those from which the

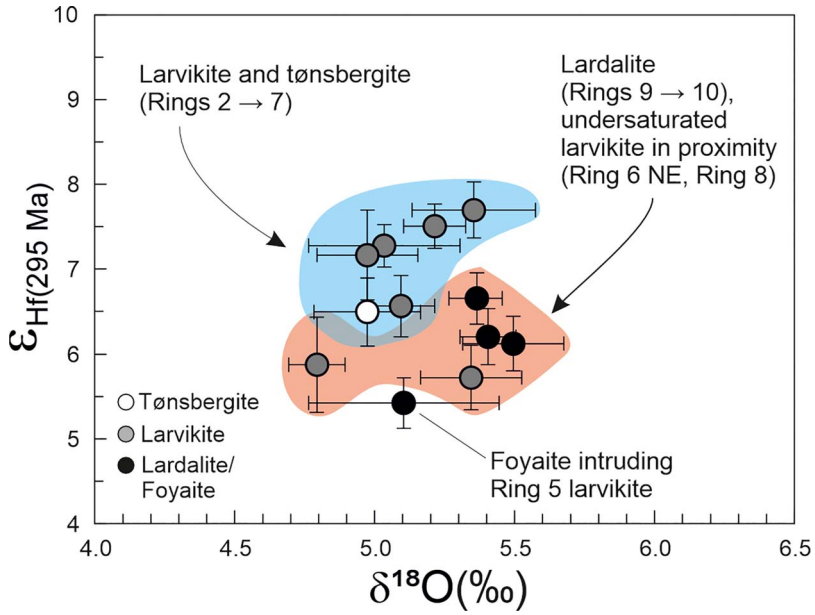

Fig. 11. $\delta^{18}O$ vs ε_{Hf} (295 Ma) diagram showing the isotope composition of the samples analyzed for both Lu–Hf- and O-in-zircon isotope composition form the Larvik plutonic complex. Monzonites (larvikite, tønsbergite) from Rings 2–7 (except those in the northeastern part of Ring 6 and Ring 8) are outlined in blue, nepheline syenites (lardalite) of Rings 9 and 10 and monzonites from the northeastern part of Ring 6 and Ring 8 in pink. Foyaite intruding larvikite in Ring 5 is marked separately. Errors are 2σ external.

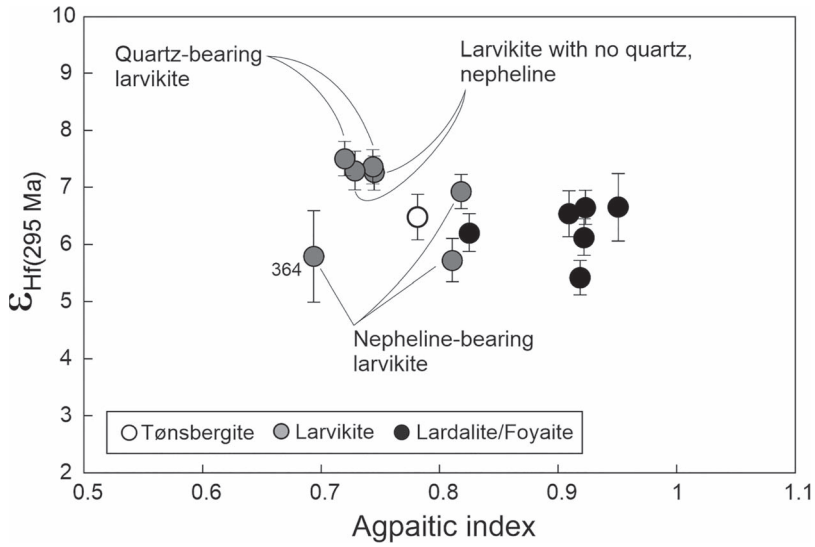

Fig. 12. Composition of tønsbergite, seven larvikites, and six lardalites/foyaites from the Larvik plutonic complex shown in an agpaitic index (molar (Na + K)/Al) vs ε_{Hf} (295 Ma) diagram. Variation in quartz and nepheline content in the larvikites (Petersen, 1978) is indicated (see also Fig. 2). Whole-rock geochemical data from Neumann (1980), Hf-isotope data on zircon from this study. Larvikite sample 364 from Ring 7 is marked. Error on ε_{Hf} is 2σ external.

nephelinites and basanites of the Skien lava series crystallized (ε_{Nd} (295 Ma) between +1 and + 2) are unlikely to be parental to the LPC, whereas basaltic members of the succession cannot be excluded. Less strongly alkaline (transitional) basalts in the Vestfold lava plateau with ε_{Nd} (295 Ma) of ~ +4 and $^{87}Sr/^{86}Sr$ (295 Ma) between 0.7035 and 0.7040 match the isotope composition of the larvikites and rhomb porphyries analyzed by Neumann *et al.* (1988) (Fig. 9).

For the Vestfold lava plateau, two basalt series were identified by Neumann *et al.* (1988), distinguished by their Ti values (in their terminology: 'HT' with $TiO_2 > 4$ wt.%, 'LT' with $TiO_2 < 4$ wt.%). These are likely to reflect different degrees of melting of a heterogeneous mantle source (Neumann *et al.*, 2002). Basalts with more than 4 wt.% TiO_2 make up a minor part of the data set of Schou-Jensen & Neumann *et al.* (1988) and Neumann *et al.* (1990, 2002) and also tend to have higher K_2O/Na_2O than basalts with lower Ti.

Neumann *et al.* (2002) noted that basalts from the Vestfold plateau with $K_2O/(Na_2O + K_2O)$ outside of the range 0.45–0.60 ($K_2O/Na_2O = 0.81$ to 1.15) also have varying concentrations of mobile trace elements, indicating alteration. Basalts with high water content (> 3 wt.%), elevated $K_2O/(Na_2O + K_2O)$, high contents of potentially mobile trace elements (e.g. Rb, Cs) and high and varying Rb/Th, Rb/Sr and initial $^{87}Sr/^{86}Sr$ ratios have certainly been modified by hydrothermal alteration or low temperature weathering. This also applies to basalts with $K_2O/(Na_2O + K_2O)$ between 0.40 and 0.45 from the Jeløy Island

(Schou-Jensen & Neumann, 1988; Neumann *et al.*, 2002). On the other hand, the published analyses of basalts with $K_2O/(Na_2O + K_2O)$ in the 0.35 to 0.40 range show narrower ranges of variation of mobile trace element values than those with $K_2O/(Na_2O + K_2O)$ between 0.45 and 0.50. We therefore regard $K_2O/(Na_2O + K_2O)$ in the range 0.35–0.4 in these basalts as a primary magmatic feature.

The volcanic rocks in the Oslo Rift are fractionated relative to their parent magmas and many show evidence of accumulation of phenocrysts. Neumann *et al.* (2002) estimated a primary magma composition for HT lavas of the Vestfold plateau (*FCI* in their Table 5) and this is our first choice as parent liquid for the LPC. No estimates of possible parent composition to the LT basalt magma have been published. The K_2O/Na_2O ratio of *FCI* (1.14) is high compared to LT basalts and the plutonic rocks of the LPC (LPC average at 0.69). A modified FCI composition, with 10% lower TiO_2 and a K_2O/Na_2O ratio of 0.61 ($K_2O/(Na_2O + K_2O) = 0.38$), with $Na_2O + K_2O$ and other paremeters kept unchanged (*modified FCI*) is also examined as a parent liquid candidate.

Other potential parent melt compositions to be considered are a basanite (*PP3*, 4.78 wt.% TiO_2) and a basalt (PP6, 3.55 wt.% TiO_2) from the Vestfold Plateau (Table 1 in Neumann *et al.*, 2002) and an alkali basalt (S55) from the Skien area (Segalstad, 1979; Anthony *et al.*, 1989), the latter with the highest ε_{Nd} (+3.4 at 295 Ma) in the data set of Dunworth *et al.* (2001). An average Skien nephelinite is also included for comparison. We will compare the Rhyolite–MELTS model residual liquids to the whole-rock major element composition of larvikite and lardalite from Neumann (1980), which includes all the samples from the G. Raade collection used in this work.

The comparatively high-pressure melt evolution regime suggested by (Neumann *et al.*, 1986) is supported by direct evidence for crystallization processes at elevated pressure in the igneous rocks of the Oslo Rift. Clinopyroxene in olivine–pyroxene cumulate xenoliths in a basalt from the Krokskogen lava plateau (Fig. 1) contains CO_2 fluid inclusions that indicate minimum trapping pressures of ≥0.55 GPa (Neumann *et al.*, 1988). The fluid inclusion assemblage of apatite in mafic cumulates (jacupirangite s.l.) entrained in larvikite in the LPC indicate trapping at magmatic temperatures between 0.5 and 0.8 GPa (Andersen & Seiersten, 1994).

Rhyolite–MELTS models: Approach and visualization

The purpose of our modeling experiment is to reproduce the overall range of compositions observed in the LPC, not the composition of individual samples. We will focus on polybaric crystallization paths in the upper mantle-lower/middle crust regime and will not consider *in situ* crystallization processes. The starting compositions (*FCI, modified FCI*, *PP3*, *PP6*, S55) were allowed to cool from a temperature well above the liquidus in 10-degree steps under isobaric conditions at pressures between 0.2 and 1 GPa, assuming complete separation of the solids (ideal fractional crystallization). All initial melt compositions were assumed to have 0.1 wt.% H_2O and the models were run at QFM oxygen fugacity, which is representative of the LPC system (Neumann, 1976). The runs were terminated when melt was consumed or at the arbitrarily chosen lower temperature limit of 1000°C. Neumann (1976) reported Mn-in-olivine temperatures of 1000–1100°C for larvikites and lardalites. These temperatures must represent an early stage of *in situ* crystallization just after emplacement and are thus estimates both of the temperature of the magma at the time of final emplacement and minimum temperature of fractionation in deeper staging chambers.

The resulting LLD are visualized in the R_1R_2 diagram of de la Roche *et al.* (1980) (Fig. 13). This diagram was chosen because it is a projection from the basalt tetrahedron with simple representation of the critical silica saturation plane (i.e. the olivine–clinopyroxene–plagioclase plane), yields a compact representation of the range of calculated melt compositions, and separates the compositions of larvikite and lardalite well. A potential parent magma for the LPC should be able to reproduce the full range of compositions by fractional crystallization under different pressure conditions, especially the large range in the R_1 parameter, which reflects the degree of silica over- and undersaturation. Further critial parameters that need to be considered are the SiO_2 content, total alkali content, the K_2O/Na_2O ratio, and the molar (Na + K)/Al ratio (agpaitic index). These parameters can be conveniently illustrated in plots against SiO_2 (Fig. 14).

Rhyolite–MELTS model results

The general range of larvikite and lardalite compositions (Fig. 13) can be accounted for by fractional crystallization of *FCI* (Fig. 13a) and *modified FCI* (Fig. 13b) parent melts at pressures between ~0.4 and ~1 GPa (for modeling results and starting compositions, see Supplementary File 4). The high-pressure trends (0.6–1 GPa) give the most strongly silica-undersaturated and alkaline fractionated melt compositions at 1000–1100°C, akin to lardalite and foyaite, whereas the lower-pressure models yield mildly under- to oversaturated larvikite-like compositions. Fractionation trends at 0.4–0.5 GPa or less lead to silica oversaturation below 1100°C, whereas trends at $P \geq \sim 0.5$ GPa remain within the silica undersaturated field (Fig. 13). The reason for this difference is a pressure-dependent effect on the fractionating mineral assemblage, with orthopyroxene crystallizing earlier at higher pressures (Fig. 15). Removal of clinopyroxene with 1 to 17% of the jadeite component (depending on pressure) followed by plagioclase gives a rising trend of K_2O/Na_2O in all of the simulations, which are reversed only when alkali feldspar or ternary feldspar starts crystallizing at temperatures between 1100°C and 1000°C (Figs 14b and 15). The FCI trends at pressures between 0.2 and 1 GPa fail to reproduce the K_2O/Na_2O of the LPC (Fig. 14a). The modified FCI gives better reproduction of the K_2O/Na_2O ratio (Fig. 14b) and also gives values for total alkali content and agpaitic index compatible with the LPC (Fig. 14c, d). The amount of the original melt remaining at the larvikite–lardalite stage with feldspar on liquidus depends on initial composition but is, in general, less than 20% at 1000–1100°C, as illustrated for LLD based on the modified FCI starting composition (Fig. 15). Cumulates formed at temperatures above 1100°C were ultramafic with olivine, pyroxene, and Fe–Ti oxides. Plagioclase and/or ternary anorthoclase cumulates could only form temperatures near 1100°C and below, that is, during the final stages of pre-emplacement melt evolution.

The Vestfold HT basanite melt (*PP3*) yields a range of silica oversaturated to mildly undersaturated liquids well within the range of larvikite compositions at 1100–1000°C at 0.5 GPa (Fig. 13a) but does not reproduce the lardalites. Skien basalt composition (S55) produces much more silica undersaturated residual liquids, matching lardalite but none of the larvikites (Fig. 13a). Both models overestimate the K_2O/Na_2O of LPC rocks (Fig. 14a). The Vestfold LT basalt composition (*PP6*) yields residuals with a more narrow range of compositions overlapping with the less silica undersaturated larvikites in Rings 2–5, but not those of Rings 6–8, nor the lardalites (Fig. 13a). It approaches the observed range of K_2O/Na_2O ratios more closely, especially at low pressure (Fig. 14a). The Skien nephelinites are ruled out on the basis of Nd isotope data (Fig. 9); a fractionation trend at 0.5 GPa from an average Skien

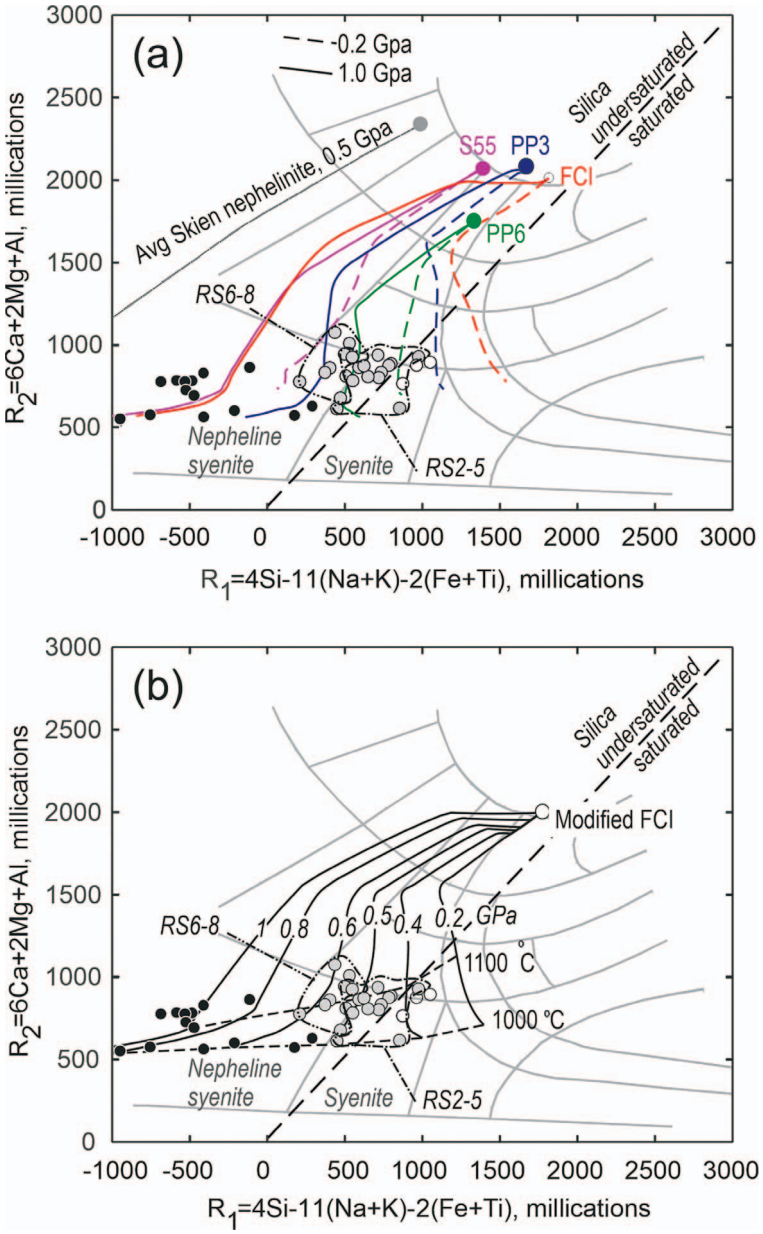

Fig. 13. R_1R_2 diagrams (de la Roche *et al.*, 1980) showing composition of tønsbergite (white circles), larvikite (gray circles), and lardalite/foyaite (black circles), with critical fractional crystallization trends from the Rhyolite-MELTS model. Compositions of larvikites from Rings 2–5 and Rings 6–8 (RS6–8 and RS2–5, respectively) are outlined, indicating the higher overall alkalinity (nepheline content) of the latter. Starting compositions and critical run results are given in Supplementary File 4. The petrographic grid of de la Roche *et al.* (1980) is shown as gray background signature, with the syenite and nepheline syenite fields indicated. The critical boundary between silica undersaturated (i.e. nepheline-bearing) and silica saturated compositions is given by a projection of the olivine-clinopyroxene-plagioclase plane in the basalt tetrahedron, which is shown as coarse-dashed line. (a) Model experiments that failed to reproduce the compositional variation in the Larvik plutonic complex include the FCI composition, which can account for the variation in the R_1 parameter, but fails to reproduce the K_2O/Na_2O of the Larvik plutonic complex (see Fig. 14a). (b) A model using the *modified FCI* composition as primary melt. This model takes into account the lower initial TiO_2 content and K_2O/Na_2O ratio of Vestfold LT basalts and LPC rocks, as discussed in the text. The two fine-dashed lines at 1100°C and 1100°C are isotherms that join model melt compositions at the given temperatures and varying pressures.

nephelinite (shown in Fig. 13a) leads toward ijolitic residual melt compositions, quite irrelevant for the LPC.

Our Rhyolite–MELTS modeling shows that polybaric fractionational crystallization of a mildly alkaline basaltic magma (cf. Neumann, 1980) will reproduce the main features of compositional variation within the LPC, within the limitations of the modeling experiment carried out in this study. Contrary to the model of Neumann (1980), however, our model allows independent, pressure-controlled LLD paths for larvikite (lower P) and lardalite and foyaite (higher P) without involving divergent secondary over- and undersaturated trends resulting from low-P fractionation.

As an alternative to polybaric crystallization of a common precursor, the present modeling results also allow for a scenario in which larvikite derives from mildly alkaline parent liquids akin to PP3 or PP6 (i.e. a Vestfold basalt source) and lardalite and foyaite from a more strongly alkaline, silica undersaturated source (S55, i.e. a Skien lava). This would, however, require parallel evolution in

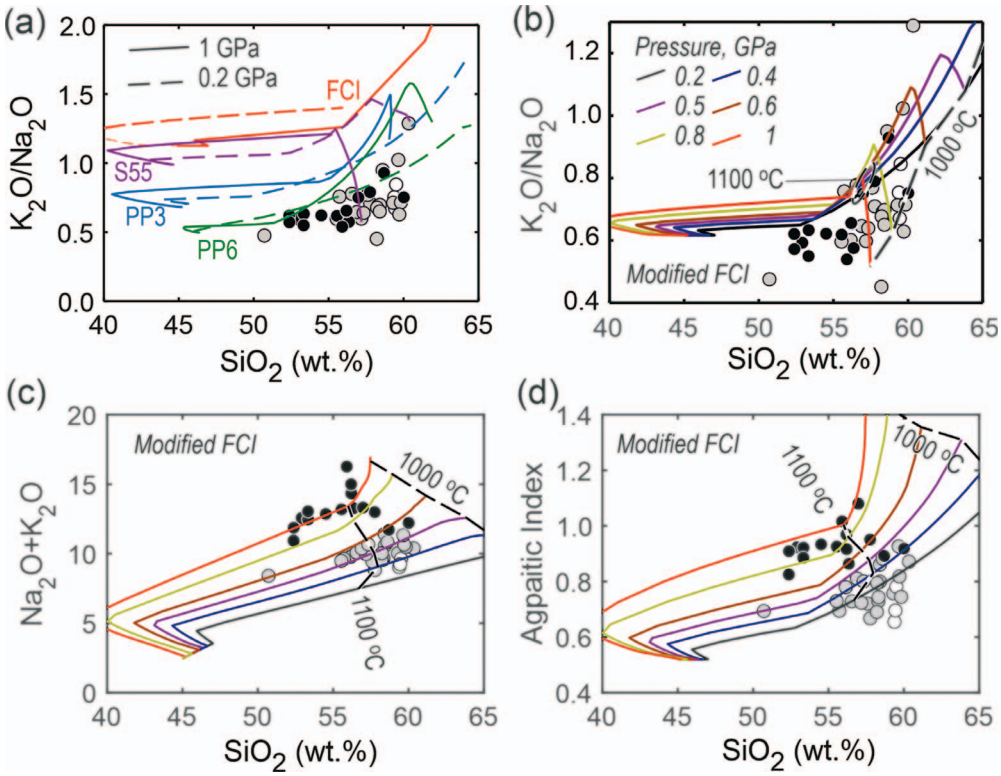

Fig. 14. Rhyolite–MELTS modeling results compared to observed rock compositions of the Larvik plutonic complex (whole-rock geochemical data from Neumann (1980); data point markers as in Fig. 13). (a) Models that fail to reproduce K_2O/Na_2O of the LPC: *FCI*, which reproduces the range of silica saturation in the complex as shown in Fig. 13a, *PP3* and S55. The 0.2-GPa trend for the PP6 composition gives a better reproduction of the observed K_2O/Na_2O but can only account for the Ring 2–5 larvikites (Fig. 13a). (b) Trends in Na_2O/K_2O vs SiO_2 at 0.2 to 1.0 GPa on the modified FCI starting melt composition, which produces liquid lines of descent compatible with the observed data. (c) Total alkali content vs SiO_2 (TAS diagram). High-pressure fractionation (0.8–1.0 GPa) accounts for the total alkali content in lardalite, fractionation at >0.2 GPa to 0.6 GPa gives residual melts with $Na_2O + K_2O$ corresponding to larvikite and tønsbergite. Color coding as in *b*. (d) Agpaitic index (AI = molar (Na + K)/Al). Fractionation at 0.8 GPa to 1.0 GPa produces residual melts with AI similar to lardalite, fractionation below 0.5 GPa give larvikite-like residual liquids. Color coding as in *b*.

independent magma chambers at pressures of ≥0.5 GPa, to agree with the independent pressure indications (Neumann *et al.*, 1988; Andersen & Seiersten, 1994). The polybaric model is favored as it is quite unlikely that the identities of the two concurrent melt lineages in the western part of the LPC would have been retained during concomitant fractionation in the lower/middle crust. It should also be noted that neither of the alternative scenarios is compatible with the alternative interpretation of geophysical data (Ebbing *et al.*, 2005), which restricts the staging chambers of the magmatic plumbing system to the upper crust. Furthermore, the Nd isotope composition of the Skien lavas is incompatible with that of the LPC (Fig. 9).

A magmatectonic model for the LPC

Opening of the Oslo Rift and decompression of the upper mantle with the formation of mildly alkaline primary melts were probably controlled by a substantial gradient in the thickness of the lithosphere (cf. Pascal *et al.*, 2004). This lithospheric step (Babuška *et al.*, 1988; Kinck *et al.*, 1993; Plomerová *et al.*, 2001) probably enhanced magma generation by focusing deformation and inducing decompression melting along the stepped zone at the lithosphere-asthenosphere transition (Pascal *et al.*, 2004). Mantle melting may have started a few million years after the onset of rifting at ~305 Ma (cf. Neumann *et al.*, 2004) and was enhanced by focused deformation as rifting proceeded. Magmas from the sublithospheric mantle invaded the crust–mantle boundary and weakened the lithosphere by localizing strain (cf. Corti *et al.*, 2003). We suggest that the LPC was fed by a mantle-derived polybaric crustal melt column in response to opening of the rift at ~58°N latitude.

An interpreted seismic section of the Oslo Rift (Fig. 16a) shows a gently up-bulging Moho underneath the rift, a ≤ 10-km-thick high-velocity mafic body in the lower crust (mafic–ultramafic cumulates; Ramberg, 1976; Neumann, 1980; Neumann *et al.*, 1986), and an intermediate to silicic (low-velocity) rock mass occupying the uppermost 5–10 km of the crust at the rift locus. According to Pascal *et al.* (2004), rifting and focusing of magmatism in the narrow rift zone was dictated by thickness contrast between western (thin) and eastern (thick) lithospheric domains and the mantle peridotite solidus was reached at the base of the lithospheric mantle soon after initiation of rifting without the need for surplus heat, resulting in relatively large-fraction decompression melting and generation of also tholeiitic primary magmas comparatively early.

The locus on mantle melting for the generation of the primary melts for the LPC was probably in a mildly depleted domain in the lithosphere-asthenosphere boundary (LAB) zone, in the upper part of the conductive sublayer (rheological boundary layer) underneath stagnant lithosphere. This marks the change from the conductive geotherm to the mantle adiabat and is characterized by both convection and conduction carrying heat throughout the region (see Sleep, 2005; Lee, 2006). The plunging LAB underneath the LPC was probably at a depth of ≥80 km (cf. Neumann *et al.*, 1992; Pedersen & van der Beek, 1994; Pascal *et al.*, 2004), which

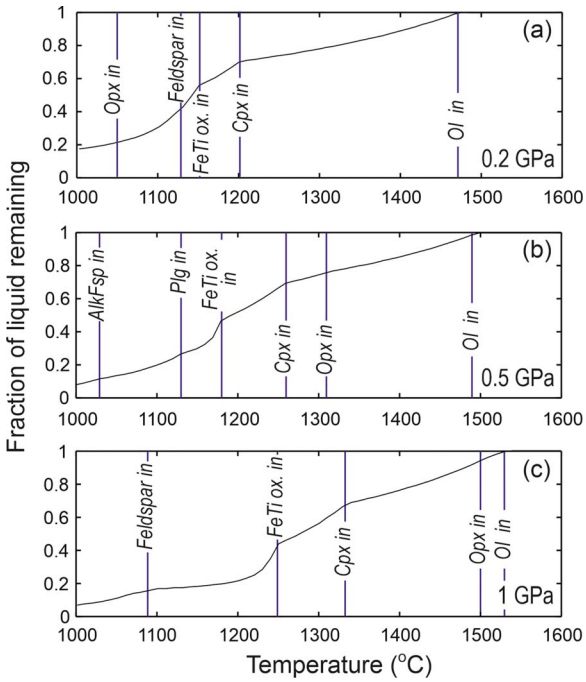

Fig. 15. Remaining liquid fraction as a function of temperature for the modified FCI initial composition at QFM oxygen fugacity and 0.1 wt.% initial water, at (a) 0.2, (b) 0.5, and (c) 1 GPa. Temperatures at which important cumulate minerals (feldspars, Fe–Ti oxide, clinopyroxene, orthopyroxene, olivine) start crystallizing are indicated. Clinopyroxene at 0.5 GPa increase in jadeite content from 0.75% at start of crystallization to 6% at 1000°C, at 1 GPa the corresponding contents of the jadeite component are 1.8 and 17%.

complies with the overall depth of peridotite solidus below lithospheric domains in Tecton settings (cf. Herzberg & Zhang, 1996; Griffin *et al.*, 1999; O'Reilly & Griffin, 2006). Small-degree melts from a HIMU-LoNd mantle source in the lithospheric mantle (cf. Anthony *et al.*, 1989; Neumann *et al.*, 2004) were also formed at an early stage of the Oslo Rift and delivered the early alkaline mafic lavas. These alkaline lavas are characterized by unradiogenic Sr isotope composition at a given Nd isotope composition as compared to the Mantle Array (cf. Hart *et al.*, 1986) and also show radiogenic Pb isotope (HIMU) characteristics as defined by Zindler & Hart (1986).

Overall, the lithospheric step beneath the rift initiated and sustained the high magma input observed (Fig. 16a; cf. Pascal *et al.*, 2004). With magma volumes building up at the LAB, strain was localized, deformation enhanced and lithosphere weakened, which then allowed development of the graben segments of the rift. The offset of maximum strain concentration between upper mantle and crust (Pascal *et al.*, 2004) may have governed the westward opening of the rift.

The first plutonic activity of the LPC was the emplacement of tønsbergite and oversaturated larvikite in the incipient rift at ~302 Ma (Fig. 16b). According to our modeling, the evolution of this magma batch involved fractionation of mildly alkaline basalt melt with final equilibration at ~0.5 GPa before emplacement. The Hf and O isotope composition of the early tønsbergite ($\varepsilon_{Hf}+6.5$, $\delta^{18}O+5$) is mantle like and contamination of these early melts by incorporation of unradiogenic Hf and ligh O from wall rocks cannot be positively verified (cf. Fig. 7b, c). The early alkaline mafic lavas of Brunlanes and Skien postdate this earliest LPC intrusion and may have extruded along large-offset boundary faults on the western margin of the incipient rift after the first intrusive event (cf. Corti, 2012). Whether or not the 304–294 Ma mænaites and camptonites that intruded into the Cambrian/Ordovician strata of the Oslofjord Supergroup (cf. Fig. 2) are related to this first larvikite injection remains unclear (cf. Sundvoll *et al.*, 1992; Sundvoll & Larsen, 1993).

As rifting continued, further intrusions of tønsbergite and quartz-bearing larvikite from the low-midcrustal melt column occurred at 299–296 Ma (Fig. 16c). This event shows progression from the east to the west (opening direction of the rift) and implies an inflation pace of ~1.5 cm/y (Fig. 16c; see also Figs. 7a, 8a), in concert with the 10-my stretching velocity of 1.6 cm/y in the model of Pascal *et al.* (2004). The Hf isotope composition of the melts may have shifted to slightly more radiogenic values with time [$\varepsilon_{Hf}+7$ (sample Bo) $\rightarrow +8$ (sample 490)] and the O isotope composition is mantle-like ($\delta^{18}O$ of 5.2‰; sample 490). This shift in the Hf isotope composition is just larger than the experimental errors involved but could point to armoring of the magma conduits and resultant reduced interaction with surrounding unradiogenic crust.

At 296 ± 1 Ma, over- to undersaturated larvikites were emplaced along the bulk of the central part of the rift (Fig. 16d). The range of ages of samples from Rings 2–6 (296.8 to 295.3 Ma) imply an enhanced opening pace (~ 3 cm/y) for the rift at this stage. The fractionating intracrustal magma column was tapped at a somewhat deeper level, possibly facilitated by increased strain affecting the rheology of the rupture zone some 5 my after the onset of rifting. The Hf and O isotope composition of these undersaturated larvikites is almost constant at $\varepsilon_{Hf} \sim +7.5$ and $\delta^{18}O \sim +5.2$‰ and shows no apparent change relative to the larvikites of the 299–296 Ma stage (Fig. 16c; Table 3).

The LPC was finalized by emplacement of two magma systems (undersaturated larvikite, lardalite/foyaite) in the western part of the complex at 296–288 Ma (Fig. 16e) and the rift attained its full width in the process. The polybaric fractionation column was tapped at different levels, delivering undersaturated monzonite (larvikite) and nepheline syenite (lardalite/foyaite) melts from shallow and deep parts of the system, respectively. The locus of emplacement of both lineages moved to the north with time (Figs 7a and 8a), larvikitic faster (~ 0.25 cm/y) than lardalitic (~ 0.1 cm/y). The faster pace of the former may reflect larger volumes of larvikite magma having been available in the shallow part of the fractionating system, whereas the deep part of the cell close to rift focus delivered to an areally more restricted emplacement system only. The two contrasting LLD retained their identity in the deviatoric stress regime of the rift, with the larvikitic lineage being a bit more radiogenic in Hf isotope composition than the lardalitic lineage. Compared to larvikite and tønsbergite in Rings 2–7, lardalites and undersaturated larvikites in the proximity of Rings 9 and 10 and the foyaite intrusive into Ring 5 have marginally lower ε_{Hf} values at a given $\delta^{18}O$ value (Fig. 11). This may indicate an isotopically a bit different (less radiogenic Hf) source having been tapped at the final stage of the buildup of the LPC.

North of the LPC, intermediate and silicic plutons were emplaced until ~260 Ma (Corfu & Larsen, 2020) but undersaturated intrusions are nonexistent. If a polybaric magma column developed in the north in the same manner, it only delivered intermediate and silicic magmas (the latter with a crustal source component; Andersen & Knudsen, 2000; see also Trønnes & Brandon, 1992) rather than nepheline syenite. The thicker continental crust in the north (Kinck *et al.*, 1993) may have prevented tapping of the deep parts of the magma column and may have caused larger crustal residence time for the mantle-derived magmas.

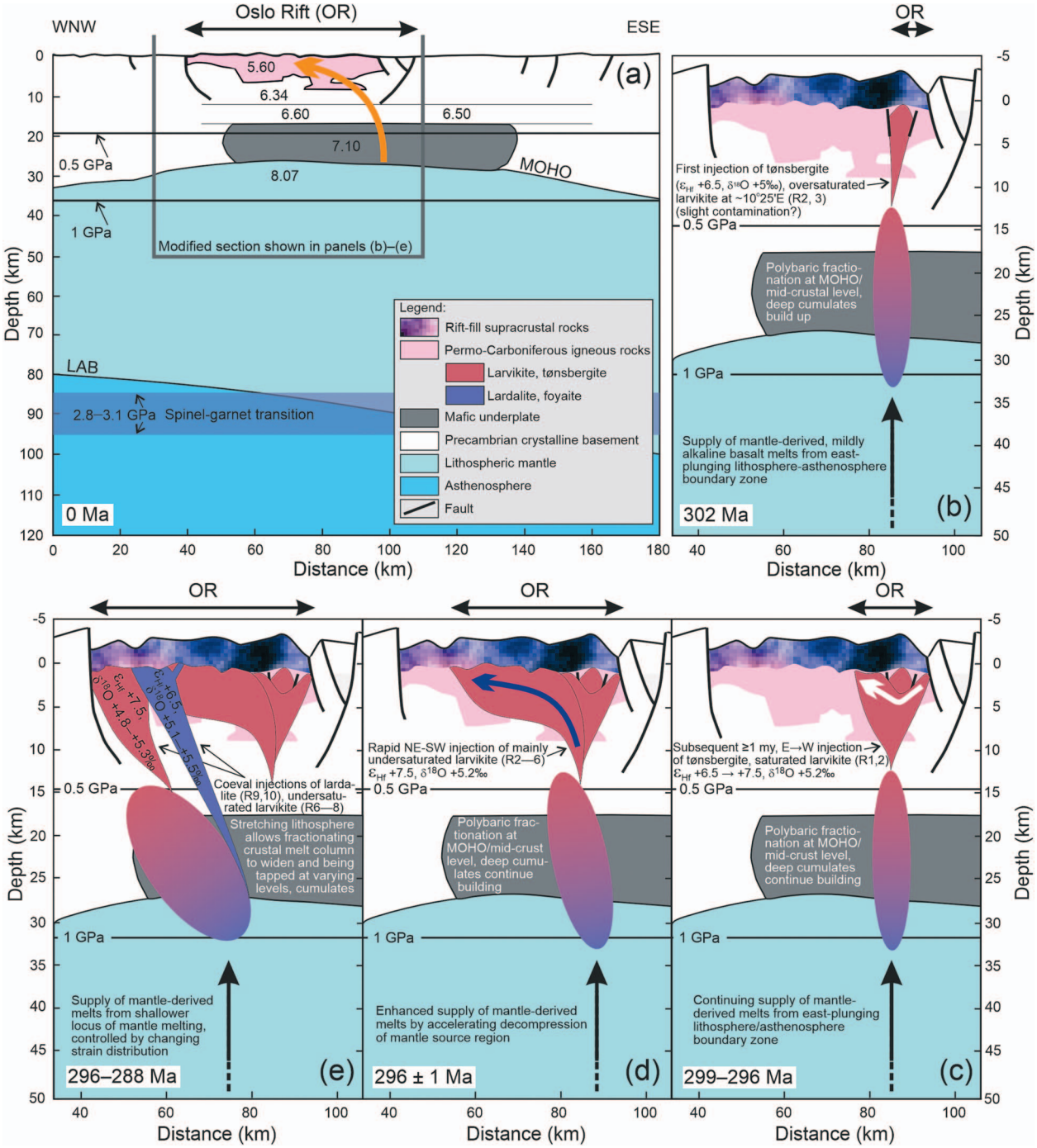

Fig. 16. Crust-upper mantle transect across the Oslo Rift and schematic magma evolution model for the 302–288-Ma Larvik plutonic complex, viewed from the SSW along the ESE-WNW profile marked in Fig. 1. (a) Interpreted seismic section modified from Neumann *et al.* (1992), Pedersen & van der Beek (1994) and Pascal *et al.* (2004). P-wave velocities in kilometer per second are shown for the upper part of the lithosphere. Moho and LAB (lithosphere-asthenosphere boundary) are marked, Moho bulging up underneath the rift and LAB plunging to the east relatively steeply. Over a distance of 250 km, the LAB deepens from 80 km at the left margin of the section to 180 km in the east, defining a major lithospheric step (Pascal *et al.*, 2004). Spinel–garnet transition at anhydrous fertile–depleted peridotite solidus is from Robinson & Wood (1998). Section enlarged in panels (b)–(e) is marked. Orange arrow indicates general direction of offset of maximum strain concentration between upper mantle and crust according to the thermo-mechanical model of Pascal *et al.* (2004). (b) First intrusion of tønsbergite and oversaturated larvikite into the incipient Oslo Rift at ~302 Ma, shown relative to the fully developed rift structure with a few km of rift-fill supracrustal rocks (now largely obliterated) and beheaded remains of plutons. (c) Emplacement of tønsbergite and oversaturated larvikite in the northeastern part of the complex with age progression from 299 to 296 Ma from the east to the west (white arrow). (d) Emplacement of mainly undersaturated larvikite accross the central part of the complex at 296 ± 1 Ma (blue arrow). (e) Concomitant intrusion of undersaturated larvikite (at 296–289 Ma) and lardalite and foyaite (at 296–288 Ma) in the western part of the complex, with locii of magmatism shifting to the approximately north (away from the viewer) with time (see Figs 7a and 8a). In (b)–(e), Hf and O isotope composition of the intrusive phases is shown, ring segments of the Larvik plutonic complex (R1–R10) shown as delineated by Petersen (1978).

Comparisons

The energy-conserved modeling done in this study lends support to a polybaric fractionation model for the intermediate plutonic rocks of the LPC first proposed by Neumann (1980). In order to produce the required range of silica saturation in the residual melts, the parent liquid must be situated very close to the silica saturation line, and close to the olivine-clinopyroxene-plagioclase plane in the basalt tetrahedron (Fig. 13). This works for starting compositions such as FCI and modified FCI (Supplementary File 4), whereas compositions further away on the undersaturated side (PP3, S55) yield silica undersaturated residual liquids, regardless of pressure. The latter seems to have been the case for the Tertiary Kangerlussuaq complex of East Greenland, which bears evidence for an alkaline basanitic/alkali olivine basalt–phonolite lineage that emerged only after magma conduit had been armored against interaction with country rocks by prolonged magmatism (Riishuus *et al.*, 2006), as well as for the Chilwa complex of Malawi that is built of sequential alkaline complexes related to a common alkaline precursor at depth (Woolley & Platt, 1986).

A different type of evolution can be seen in the Gardar Rift of South Greenland. The parent magma of the US plutonic rocks of the Gardar Rift was probably also a transitional olivine basalt close to the olivine–clinopyroxene–plagioclase plane, but with distinctly higher Al_2O_3/CaO than any of the potential parent liquids in the Oslo Rift (cf. Upton, 2013). Such a parent magma would precipitate plagioclase at a much earlier stage of the crystallization history than the LPC magma, driving residuals toward increasing silica undersaturation. Deep crustal cumulates in the Gardar Rift consist of anorthosite and gabbroic rocks, which are well represented in the xenolith material from Gardar (Bridgwater & Harry, 1968). In contrast, ultramafic to mafic cumulates are expected in the Oslo Rift from the relationships in Fig. 16, which is supported by the scanty xenolith evidence available (Neumann *et al.*, 1988). Our polybaric fractionation model may thus explain the existence of cogenetic OS-US rock assemblages only if primary magma compositions are located within a narrow window on the silica-undersaturated side of the olivine-clinopyroxene–plagioclase plane in the basalt tetrahedron, and plagioclase is not an early crystallizing mineral.

Among Late Precambrian–Paleozoic OS–US complexes, the LPC is a rare, if not unique, example of successive emplacement of centered complexes in the direction of opening of a continental rift. For example, in the Gardar Rift of South Greenland, along the boundary zone of Archean and Proterozoic lithospheric domains, two distinct rifting events (older Gardar at ~1300 Ma, younger Gardar at ~1150 Ma) affected the South Greenland crystalline basement (Upton, 2013). Younger Gardar is marked by the emplacement of two mafic (transitional basaltic) giant dike complexes and alkaline (largely syenitic and nepheline syenitic) central-type intrusive complexes were emplaced in post-extensional stage and do not show within-complex age progression comparable to the LPC (Upton *et al.*, 2003; Upton, 2013).

As the LPC was emplaced, the east–west opening of the incipient Oslo Rift involved enhancing magma production and tapping of the deeper parts of the resulting magma column with time, as well as growth of the LPC in an almost linear manner in that direction at ~59°N latitude. These are unique features of the LPC, probably driven by the marked lithospheric step at the locus of the Oslo Rift. Many of the Phanerozoic central complexes in intracontinental settings, for instance the Younger Granites of Nigeria, show distinct magmatic emplacement tracks comparable to that of the LPC (e.g. Turner, 1963; Turner & Bowden, 1979; Rahaman *et al.*, 1984; Kamaunji *et al.*, 2020). They are, however, more silicic, their magmatic evolution had a more pronounced low-P component, and they were emplaced at relatively low pace, probably along deep-seated transcurrent faults mid-plate of a stabilized orogen – not in an opening rift at a major lithospheric discontinuity (cf. Bowden & Kinnaird, 1984; Rahaman *et al.*, 1984; Pitcher, 1993).

CONCLUDING REMARKS

Petersen (1978) showed that the LPC is a Paleozoic ring complex consisting of numerous, roughly circular sections almost across the width of the rift. He also showed that the igneous activity of the complex probably moved westward with time and that multiple magma batches were injected along the path of igneous activity, possibly associated with cauldron subsidence. Combined with U–Pb ages quoted in more recent abstracts and reports (Dahlgren *et al.*, 1996, 1998; Dahlgren, 2010), our data refine the temporal evolution of the LPC and set a time frame for the westward migration of magmatism (from 299 to 289 Ma) and imply two consanguineous, relatively young (~296–288 Ma) emplacement sequences in the western part of the complex. The framework of ten ring structures of Petersen (1978) may be an oversimplification of the actual magma emplacement system of the LPC that, according to our observations, involved emplacement of an early, now almost eradicated, oversaturated larvikite–tønsbergite in the eastern part of the complex, a major larvikitic melt volume after ~5 my of inception, and two consanquineous lineages (larvikite, lardalite) in the western part of the complex. The structure of the LPC was presumably continuously modified during build-up, involving differential movements of upper crustal blocks in response to magma injection to subvolcanic level, advancing extension, and cannibalism of pre-existing cauldrons by invading melt batches from the fractionating melt column. In the course of the opening of the rift, the melt column was tapped at successively deeper levels and the melts evolved with no marked crustal contamination, retaining their mantle-derived isotope composition.

FUNDING

This work was supported by the Academy of Finland (project 1131018,'A-type Granites and Related Rocks: Southern Laurentia and the Oslo Rift', to OTR), the Swedish Research Council (infrastructure grant 2014–06375), and the University of Iceland. The Department of Geosciences, University of Oslo, gave economic support for oxygen isotope analysis.

DATA AVAILABILITY

The data in this article are available in the article and in its online supplementary material.

SUPPLEMENTARY DATA

Supplementary files and figures are available at *Journal of Petrology* online.

ACKNOWLEDGMENTS

We thank Emmi Annanolli (neé Miettinen) for performing the heavy mineral separations at the Department of Geosciences, University of Oslo, and Jarkko Lamminen for providing help and

instructions. Siri Simonsen and Magnus Kristoffersen assisted in the mass spectrometer lab. We are thoroughly grateful to Carol Frost, Fernando Corfu, and Tod Waight for their insightful journal reviews. Discussions with Johanna Salminen are appreciated. This is NordSIMS publication number 720.

References

Andersen, T. (2014). The detrital zircon record: supercontinents, parallel evolution—or coincidence? *Precambrian Research* **244**, 279–287. https://doi.org/10.1016/j.precamres.2013.10.013.

Andersen, T. & Elburg, M. A. (2022). Open-system behaviour of detrital zircon during weathering: an example from the Palaeoproterozoic Pretoria group, South Africa. *Geological Magazine* **159**(4), 561–576. https://doi.org/10.1017/S001675682100114X.

Andersen, T. & Knudsen, T.-L. (2000). Crustal contaminants in the Permian Oslo rift, South Norway: constraints from Precambrian geochemistry. *Lithos* **53**, 247–264. https://doi.org/10.1016/S0024-4937(00)00028-1.

Andersen, T. & Seiersten, M. (1994). Deep cumulates in a shallow intrusion: origin and crystallization history of a pyroxenite (jacupirangite s.l.) body in the Larvik pluton, Oslo region, South Norway. *Neues Jahrbuch für Mineralogie, Monatshefte* **6**, 255–274.

Andersen, T., Andresen, A. & Sylvester, A. G. (2001). Nature and distribution of deep crustal reservoirs in the southwestern part of the Baltic shield: evidence from Nd, Sr, and Pb isotope data on late Sveconorwegian granites. *Journal of the Geological Society, London* **158**, 253–267. https://doi.org/10.1144/jgs.158.2.253.

Andersen, T., Griffin, W. L. & Pearson, N. J. (2002). Crustal evolution in the SW part of the Baltic shield: the Hf isotope evidence. *Journal of Petrology* **43**(9), 1725–1747. https://doi.org/10.1093/petrology/43.9.1725.

Andersen, T., Griffin, W. L., Jackson, S. E., Knudsen, T.-L. & Pearson, N. J. (2004). Mid-Proterozoic magmatic arc evolution at the southwestern margin of the Baltic shield. *Lithos* **73**, 289–318. https://doi.org/10.1016/j.lithos.2003.12.011.

Andersen, T., Andersson, U. B., Graham, S., Åberg, G. & Simonsen, S. L. (2009). Granitic magmatism by melting of juvenile continental crust: new constraints on the source of Palaeoproterozoic granitoids in Fennoscandia from Hf isotopes in zircon. *Journal of the Geological Society, London* **166**, 233–247. https://doi.org/10.1144/0016-76492007-166.

Andersen, T., Elburg, M. A. & Van Niekerk, H. S. (2019). Detrital zircon in sandstones from the Palaeoproterozoic Waterberg and Nylstroom basins, South Africa: provenance and recycling. *South African Journal of Geology* **122**(1), 79–96. https://doi.org/10.25131/sajg.122.0008.

Anthony, E. Y., Segalstad, T. V. & Neumann, E.-R. (1989). An unusual mantle source region for nephelinites from the Oslo rift, Norway. *Geochimica et Cosmochimica Acta* **53**, 1067–1076. https://doi.org/10.1016/0016-7037(89)90211-1.

Artemieva, I. M. & Meissner, R. (2012). Crustal thickness controlled by plate tectonics: a review of crust-mantle interaction processes illustrated by European examples. *Tectonophysics* **530-531**, 18–49. https://doi.org/10.1016/j.tecto.2011.12.037.

Ashwal, L., Torsvik, T., Horváth, P., Harris, C., Webb, S., Werner, S. & Corfu, F. (2016). A mantle-derived origin for Mauritian Trachytes. *Journal of Petrology* **57**, egw052–egw1675. https://doi.org/10.1093/petrology/egw052.

Aspin, A. (2016). *High-Impact data Visualization in Excel with Power View, 3D Maps, Get & Transform and Power BI*. Berkeley: Apress, ISBN-13 (electronic) 978–1–4842-2400-7, https://doi.org/10.1007/978-1-4842-2400-7.

Babuška, V., Plomerová, J. & Padjušak, P. (1988). Seismologically determined deep lithosphere structure in Fennoscandia. *Geologiska Föreningens i Stockholm Förhandlingar* **110**, 380–382. https://doi.org/10.1080/11035898809452676.

Barnes, C. G., Coint, N., Barnes, M. A., Chamberlain, K. M., Cottle, J. M., Rämö, O. T., Strickland, A. & Valley, J. W. (2021). Open-system evolution of a crustal-scale magma column, Klamath Mountains, California. *Journal of Petrology* **62**(12), 1–29. https://doi.org/10.1093/petrology/egab065.

Barth, T. F. W. (1945). Studies on the igneous rock complex of the Oslo region. II. Systematic petrography of the plutonic rocks. *Skrifter utgitt av Det Norske Videnskaps-Akademi i Oslo. I.Matematisk-Naturvitenskapelig klasse 1944* , No. 9.

Bergstøl, S. (1972). The jacupirangite at Kodal, Vestfold, Norway. *Mineralium Deposita* **7**, 233–246. https://doi.org/10.1007/BF00206786.

Bingen, B., Davis, W. J., Hamilton, M. A., Engvik, A., Stein, H. J., Skår, Ø. & Nordgulen, Ø. (2008). Geochronology of high-grade metamorphism in the Sveconorwegian belt, S. Norway: U-Pb, Th-Pb and re-Os data. *Norwegian Journal of Geology* **88**, 13–42.

Black, L. P., Kamo, S. L., Allen, C. M., Davis, D. W., Aleinikoff, J. N., Valley, J. W., Mundil, R., Campbell, I. H., Korsch, R. J., Williams, I. S. & Foudoulis, C. (2004). Improved $^{206}Pb/^{238}U$ microprobe geochronology by the monitoring of a trace-element-related matrix effect; SHRIMP, ID–TIMS, ELA–ICP–MS and oxygen isotope documentation for a series of zircon standards. *Chemical Geology* **205**(1–2), 115–140. https://doi.org/10.1016/j.chemgeo.2004.01.003.

Bouvier, A., Vervoort, J. D. & Patchett, P. J. (2008). The Lu–Hf and Sm–Nd isotopic composition of CHUR: constraints from unequilibrated chondrites and implications for the bulk composition of terrestrial planets. *Earth and Planetary Science Letters* **273**, 48–57. https://doi.org/10.1016/j.epsl.2008.06.010.

Bowden, P. & Kinnaird, J. A. (1984). The petrology and geochemistry of alkaline granites from Nigeria. *Physics of the Earth and Planetary Interiors* **35**, 199–211. https://doi.org/10.1016/0031-9201(84)90043-8.

Bridgwater, D. & Harry, W. T. (1968). Anorthosite xenoliths and plagioclase megacrysts in Precambrian intrusions of South Greenland, part 1. *Meddelelser om Grønland* **77**(2), 1–243. https://doi.org/10.34194/bullggu.v77.6617.

Brøgger, W. C. (1886). Über die Bildunggsgeschichte des Kristiana-Fjords. *Nyt Magazin for Naturvidenskaberne* **30**, 99–231.

Brøgger, W. C. (1890). Die Mineralien der Syenitpegmatitgänge der südnorwegischen Augit- and Nephelinsyenite. *Zeitschrift für Kristallographie* **16**, 1-235–1-663.

Brøgger, W. C. (1898). Die Eruptivgesteine des Oslogebietes III. *Die Ganggefolke des Laurdaliths. Skrifter utgitt av Det Norske Videnskaps-Akademi i Oslo I. Matematisk-Naturvitenskapelig klasse 1897* , No. 6.

Brøgger, W. C. (1906). Eine Sammlung der wichtigsten Typen der Eruptivgesteine des Kristianiagebietes nach ihren geologischen Verwandschaftsbeziehungen geordnet. *Nyt Magazin for Naturvidenskaberne* **44**(2), 113–144.

Brøgger, W. C. (1933). Die Eruptivgesteine des Oslogebietes VII. *Die chemische Zusammen setzung der Eruptivegesteine des Oslogebietes. Skrifter utgitt av Det Norske Videnskaps-Akademi i Oslo I. Matematisk-Naturvitenskapelig klasse 1933* , No. 1.

Buck, W. R. (1991). Modes of continental lithospheric extension. *Journal of Geophysical Research* **96**(B12), 20161–20178. https://doi.org/10.1029/91JB01485.

Corfu, F. & Dahlgren, S. (2008). Perovskite U-Pb ages and the Pb isotopic composition of alkaline volcanism initiating the Permo-Carboniferous Oslo rift. *Earth and Planetary Science Letters* **265**, 256–269. https://doi.org/10.1016/j.epsl.2007.10.019.

Corfu, F. & Larsen, B. T. (2020). U-Pb systematics in volcanic and plutonic rocks of the Krokskogen area: resolving a 40 million years long evolution in the Oslo rift. *Lithos* **376-377**, 105755. https://doi.org/10.1016/j.lithos.2020.105755.

Corti, C. (2012). Evolution and characteristics of continental rifting: Analog modeling-inspired view and comparison with examples from the east African rift system. *Tectonophysics* **522-523**, 1–33. https://doi.org/10.1016/j.tecto.2011.06.010.

Corti, C., Bonini, M., Conticelli, S., Innocenti, F., Manetti, P. & Sokoutos, D. (2003). Analogue modelling of continental extension: a review focused on the relations between the patterns of deformation and the presence of magma. *Earth-Science Reviews* **63**, 169–247. https://doi.org/10.1016/S0012-8252(03)00035-7.

Dahlgren, S. (2010) The Larvik plutonic complex: The larvikite and nepheline syenite plutons and their pegmatites. In: Larsen A. O. (ed) *The Langensundsfjord: History, Geology, Pegmatites, Minerals*. Salzhemmendorf, Germany: Bode, pp. 26–37.

Dahlgren, S., Corfu, F. & Heaman, L. M. (1996). U-Pb isotopic time constraints, and Hf and Pb source chatacteristics of the Larvik plutonic complex, Oslo paleorift. Geodynamic and geochemical implications for the rift evolution. *V.M. Goldsschmidt Conference Abstracts* **1**, 120.

Dahlgren, S., Corfu, F. & Heaman, L. M. (1998). Datering av plutoner og pegmatitter i Larvik pluton-kompleks, sydlige Oslo graben, ved hjelp av U-Pb isotoper i zircon og baddeleyitt. *Norsk Bergverksmuseum Skrift* **14**, 32–39 [in Norwegian].

Derby, O. A. (1891). On the magnetite ore districts of Jacupiranga and Ipanema, São Paulo, Brazil. *American Journal of Science* **s3-41**(244), 311–321. 10.2475/ajs.s3-41.244.311.

Dunworth, E. A., Neumann, E.-R. & Rosenbaum, J. M. (2001). The Skien lavas, Oslo rift: petrological disequilibrium and geological evolution. *Contributions to Mineralogy and Petrology* **140**, 701–719. https://doi.org/10.1007/s004100000215.

Ebbing, J., Afework, Y., Olesen, O. & Nordgulen, Ø. (2005). Is there evidence for magmatic underplating beneath the Oslo rift? *Terra Nova* **17**, 129–134. https://doi.org/10.1111/j.1365-3121.2004.00592.x.

Elburg, M. A., Andersen, T., Bons, P. D., Simonsen, S. L. & Weisheit, A. (2013). New constraints on Phanerozoic magmatic and hydrothermal events in the Mt Painter Province, South Australia. *Gondwana Research* **24**, 700–712. https://doi.org/10.1016/j.gr.2012.12.017.

Foland, K. A., Landoll, J. D., Henderson, C. M. B. & Jiangfeng, C. (1993). Formation of cogenetic quartz and nepheline syenites. *Geochimica et Cosmochimica Acta* **57**, 697–704. https://doi.org/10.1016/0016-7037(93)90380-F.

Gabrielsen, R. H., Nystuen, J. P. & Olesen, O. (2018). Fault distribution in the Precambrian basement of South Norway. *Journal of Structural Geology* **108**, 269–289. https://doi.org/10.1016/j.jsg.2017.06.006.

Griffin, W. L., O'Reilly, S. Y. & Ryan, C. G. (1999) The composition and origin of sub-continental lithospheric mantle. In: Fei Y., Bertka C. M. & Mysen B. O. (eds) *Mantle Petrology: Field Observations and High Pressure Experimantation: A Tribute to Francis R. (Joe) Boyd*. Alexandria: The Geochemical Society, Special Publication 6, pp. 13–45.

Griffin, W. L., Pearson, P. J., Belousova, E., Jackson, S. E., van Achterberg, E., O'Reilly, S. Y. & Shee, S. R. (2000). The Hf isotope composition of cratonic mantle: LAM-MC-ICPMS analysis of zircon megacrysts in kimberlites. *Geochimica et Cosmochimica Acta* **64**, 133–147. https://doi.org/10.1016/S0016-7037(99)00343-9.

Groome, N. T. (2017) *A description of the Bjønnes nepheline syenite intrusion, part of the Larvik plutonic complex, Norway*. Unpublished M.Sc. thesis. Norway: Department of Geosciences, University of Oslo.

Gualda, G. A. R. & Ghiorso, M. S. (2015). MELTS_Excel: A Microsoft Excel-based MELTS interface for research and teaching of magma properties and evolution. *Geochemistry, Geophysics, Geosystems* **16**(1), 315–324. https://doi.org/10.1002/2014GC005545.

Gualda, G. A. R., Ghiorso, M. S., Lemons, R. V. & Carley, T. L. (2012). Rhyolite-MELTS: a modified calibration of MELTS optimized for silica-rich, fluid-bearing magmatic systems. *Journal of Petrology* **53**, 875–890. https://doi.org/10.1093/petrology/egr080.

Hart, S. R., Gerlach, D. C. & White, W. M. (1986). A possible new Sr-Nd-Pb mantle array and consequences for mantle mixing. *Geochimica et Cosmochimica Acta* **50**, 1551–1557. https://doi.org/10.1016/0016-7037(86)90329-7.

Heinonen, A. P., Andersen, T. & Rämö, O. T. (2010). Re-evaluation of rapakivi petrogenesis: source contrains from the Hf isotope composition of zircon in the rapakivi granites and associated mafic rocks of southern Finland. *Journal of Petrology* **51**, 1687–1709. https://doi.org/10.1093/petrology/egq035.

Heinonen, A., Andersen, T., Rämö, O. T. & Whitehouse, M. J. (2015). The source of Proterozoic anorthosite and rapakivi granite magmatism: evidence from combined in situ Hf–O isotopes of zircon in the Ahvenisto complex, southeastern Finland. *Journal of the Geological Society* **172**, 103–112. https://doi.org/10.1144/jgs2014-013.

Henderson, C. M. B. (1984). Feldspathoid stabilities and phase inversions – a review. In: Brown, W. L. (ed.) *Feldspars and Feldspathoids*. Dordrecht. Springer Netherlands, 471–499, https://doi.org/10.1007/978-94-015-6929-3_13.

Huhma, H., Mänttäri, I., Peltonen, P., Kontinen, A., Halkoaho, T., Hanski, E., Hokkanen, T., Hölttä, P., Juopperi, H., Konnunaho, J., Layahe, Y., Luukkonen, E., Pietikäinen, K., Pulkkinen, A., Sorjonen-Ward, P., Vaasjoki, M. & Whitehouse, M. (2012). The age of the Archaean greenstone belts in Finland. *Geological Survey of Finland, Special Paper* **54**, 74–175.

Jackson, S. E., Pearson, N. J., Griffin, W. L. & Belousova, E. A. (2004). The application of laser ablation-inductively coupled plasma-massspectrometry to in situ U–Pb zircon geochronology. *Chemical Geology* **211**, 47–69. https://doi.org/10.1016/j.chemgeo.2004.06.017.

Jaffey, A. H., Flynn, K. F., Glendenin, L. E., Bentley, W. C. & Essling, A. M. (1971). Precision measurement of half-lives and specific activities of ^{235}U and ^{238}U. *Phys Rev C* **4**, 1889–1906. https://doi.org/10.1103/PhysRevC.4.1889.

Janoušek, V., Farrow, C. M. & Erban, V. (2006). Interpretation of whole-rock geochemical data in igneous geochemistry: introducing Geochemical Data Toolkit (GCDkit). *Journal of Petrology* **47**(6), 1255–1259. https://doi.org/10.1093/petrology/egl013.

Janoušek, V., Moyen, J. F., Martin, H., Erban, V. & Farrow, C. (2016). Geochemical Modelling of Igneous Processes –Principles and Recipes in R Language. *Bringing the Power of R to a Geochemical Community*. Springer-Verlag, Berlin, Heidelberg; https://doi.org/10.1007/978-3-662-46792-3

Johnson, C. M. & Beard, B. L. (1993). Evidence from hafnium isotopes for ancient sub-oceanic mantle beneath the Rio Grande rift. *Nature* **362**, 441–444. https://doi.org/10.1038/362441a0.

Kamaunji, V. D., Wang, L.-X., Ahmed, H. A., Zhu, Y.-X., Vincent, V. I. & Girei, M. B. (2020). Coexisting A1 and A2 granites of Kudaru complex: implications for genetic and tectonic diversity of a-type granite in the younger granite province, north-central Nigeria. *International Journal of Earth Sciences* **109**, 511–535. https://doi.org/10.1007/s00531-020-01818-8.

Keller, G. R., Khan, M. A., Morgan, P., Wendlandt, R. F., Baldridge, W. S., Olsen, K. H., Prodehl, C. & Braile, L. W. (1991). A comparative study of the Rio Grande and Kenya rifts. *Tectonophysics* **197**, 355–371. https://doi.org/10.1016/0040-1951(91)90050-3.

Kinck, J. J., Husebye, E. S. & Larsson, F. R. (1993). The Moho depth distribution in Fennoscandia and the regional tectonic evolution from Archean to Permian times. *Precambrian Research* **64**, 23–51. https://doi.org/10.1016/0301-9268(93)90067-C.

Košler, J. (2008) Laser ablation sampling strategies for concentration and isotope ratio analyses by ICP-MS. In: Sylvester P. (ed) *Laser Ablation–ICP–MS in the Earth Sciences: Current Practices and Outstanding Issues. Mineralogical Association of Canada Short Course Series 40*. Québec: Mineralogical Association of Canada/Association Minéralogique du Canada, pp. 79–92.

Larsen, B. T., Olaussen, S., Sundvoll, B. & Heeremans, M. (2008). The Permo-carboniferous Oslo rift through six stages and 65 million years. *Episodes* **31**, 52–58. https://doi.org/10.18814/epiiugs/2008/v31i1/008.

Le Maitre, R. W., Streckeisen, A., Zanettiun, B., LeBas, M. J., Bonin, B., Bateman, P., Bellieni, G., Dudek, A., Efremova, S., Keller, J., Lameyre, J., Sabine, P. A., Schmid, R., Sørensen, H. & Woolley, A. R. (2002). *Igneous rocks. A classification and glossary of terms*. Cambridge University Press, Cambridge, U.K, https://doi.org/10.1017/CBO9780511535581.

Le Masurier, W., Futa, K., Hole, M. & Kawachi, Y. (2003). Polybaric evolution of phonolite, trachyte, and rhyolite volcanoes in eastern Marie Byrd Land, Antarctica: controls on peralkalinity and silica saturation. *International Geology Review* **45**, 1055–1099. https://doi.org/10.2747/0020-6814.45.12.1055.

Leake, B. E., Woolley, A. R., Arps, C. E. S., Birch, W. D., Gilbert, M. C., Grice, J. D., Hawthorne, F. C., Kato, A., Kisch, H. J., Krivovichev, V. G., Linthout, K., Laird, J., Mandarino, J. A., Maresch, W. V., Nickel, E. H., Rock, N. M. S., Schumacher, J. C., Smith, D. C., Stephenson, N. C. N., Ungaretti, L., Whittaker, E. J. W. & Youzhi, G. (1997). Nomenclature of amphiboles: report of the subcommittee on amphiboles of the International Mineralogical Association, commission on new minerals and mineral names. *Canadian Mineralogist* **35**(1), 219–246.

Lee, C.-T. A. (2006). Geochemical/petrologic constraints on the origin of cratonic mantle. *Archean Geodynamics and Environments* **164**, 89–114. https://doi.org/10.1029/164GM08.

Herzberg, C. & Zhang, J. (1996). LPC written out Melting experiments on anhydrous peridotite KLB-1 Compositions of magmas in the upper mantle and transition zone. *Journal of Geophysical Research* **101**, 8271–8295.

Ludwig, K. R. (1998). On the treatment of concordant uranium-lead ages. *Geochimica et Cosmochimica Acta* **62**, 665–676. https://doi.org/10.1016/S0016-7037(98)00059-3.

Ludwig, K. R. (2003) *Isoplot 3.0—a geochronological toolkit for Microsoft Excel*. Berkeley Geochronology Center Special Publication no. 4.

Lutro, O. & Nordgulen, Ø. (2008). Oslofeltet, berggrunnskart, scale 1:250,000. *Norges Geologiske Undersøkelse*, Trondheim, Norway.

Morgan, P. & Baker (1983). Processes of continental rifting. *Tectonophysics* **94**, 1–10. https://doi.org/10.1016/0040-1951(83)90005-7.

Morimoto, N., Faøies, J., Ferguson, A. K., Ginzburg, I. V., Ross, M., Seifeit, F. A. & Zussman, J. (1989). Nomenclature of pyroxenes. *Canadian Mineralogist* **14**, 198–221. https://doi.org/10.2465/minerj.14.198.

Nasdala, L., Reiners, P. W., Garver, J. I., Kennedy, A. K., Stern, R. A., Balan, E. & Wirth, R. (2004). Incomplete retention of radiation damage in zircon from Sri Lanka. *American Mineralogist* **89**, 219–231. https://doi.org/10.2138/am-2004-0126.

Neumann, E.-R. (1976). Compositional relations among pyroxenes, amphiboles and other mafic phases in the Oslo region plutonic rocks. *Lithos* **9**, 85–109. https://doi.org/10.1016/0024-4937(76)90028-1.

Neumann, E.-R. (1980). Petrogenesis of the Oslo region larvikites and associated rocks. *Journal of Petrology* **21**(3), 499–531.

Neumann, E.-R., Larsen, B. T. & Sundvoll, B. (1985). Compositional variations among gabbroic intrusions in the Oslo rift. *Lithos* **18**, 35–59. https://doi.org/10.1016/0024-4937(85)90005-2.

Neumann, E.-R., Pallesen, S. & Andresen, P. (1986). Mass estimates of cumulates and residues after anatexis in the Oslo graben. *Journal of Geophysical Research* **91**(B11), 11629–11640. https://doi.org/10.1029/JB091iB11p11629.

Neumann, E.-R., Tilton, G. R. & Tuen, E. (1988). Sr, Nd, and Pb isotope geochemistry of the Oslo rift igneous province, Southeast Norway. *Geochimica et Cosmochimica Acta* **52**, 1997–2007. https://doi.org/10.1016/0016-7037(88)90180-9.

Neumann, E.-R., Sundvoll, B. & Øverli, P. E. (1990). A mildly depleted upper mantle beneath Southeast Norway: evidence from basalts in the Permo-carboniferous Oslo rift. *Tectonophysics* **178**, 89–107. https://doi.org/10.1016/0040-1951(90)90461-G.

Neumann, E.-R., Olsen, K. H., Baldridge, W. S. & Sundvoll, B. (1992). The Oslo rift: a review. *Tectonophysics* **208**, 1–18. https://doi.org/10.1016/0040-1951(92)90333-2.

Neumann, E.-R., Dunworth, E. A., Sundvoll, B. A. & Tollefsrud, J. I. (2002). B1 basaltic lavas in Vestfold-Jeløya area, Central Oslo rift: derivation from initial melts formed by progressive partial melting of an enriched mantle source. *Lithos* **61**, 21–53. https://doi.org/10.1016/S0024-4937(02)00068-3.

Neumann, E.-R., Wilson, M., Heeremans, M., Spencer, E., Obst, K., Timmerman, M. J. & Kirstein, L. (2004). *Carboniferous-Permian rifting and magmatism in southern Scandinavia, the North Sea and Northern Germany: A review*. In: Wilson, M., Neumann, E.-R., Davies, G. R., Timmerman, M. J., Heeremans, M. & Larsen, B. T. (eds.) *Permo-Carboniferous magmatism and rifting in Europe*. London: Geological Society, London, Special Publications **223**, 11–40, https://doi.org/10.1144/GSL.SP.2004.223.01.02.

O'Reilly, S. Y. & Griffin, W. L. (2006). Imaging global chemical and thermal heterogeneity in the subcontinental lithospheric mantle with garnets and xenoliths: geophysical implications. *Tectonophysics* **416**, 289–309. https://doi.org/10.1016/j.tecto.2005.11.014.

Oftedahl, C. (1952). Studies on the igneous rock complex of the Oslo region. *XII The Lavas. Skrifter utgitt av Det Norske Videnskaps-Akademi i Oslo. I. Matematisk-Naturvitenskapelig klasse* **1952**, 3.

Oftedahl, C. & Petersen, J. S. (1978). Southern part of the Oslo rift. *Norges Geologiske Undersøkelse Bulletin* **337**, 163–182.

Olsen, M. T. (2018) *Opprinnelsen og aldermen til de yngste felsiske plutonene i Oslofeltet – En LAM-MC-ICPMS U-Pb og Lu-Hf-isotopstudie av zircon*Unpublished M.Sc. thesis. Norway: Department of Geosciences, University of Oslo, in Norwegian.

Pascal, C., Cloeting, S. A. P. L. & Davies, G. R. (2004). *Asymmetric lithosphere as the cause of rifting and magmatism in the Permo-Carboniferous Oslo Graben*. In: Wilson, M., Neumann, E.-R., Davies, G. R., Timmerman, M. J., Heeremans, M. & Larsen, B. T. (eds.) *Permo-Carboniferous magmatism and rifting in Europe*. London: Geological Society, London, Special Publications **223**, 139–156, https://doi.org/10.1144/GSL.SP.2004.223.01.06.

Pedersen, T. & van der Beek, P. (1994). Extension and magmatism in the Oslo rift, Southeast Norway: no sign of a mantle plume. *Earth and Planetary Science Letters* **123**, 317–329. https://doi.org/10.1016/0012-821X(94)90276-3.

Pedersen, L. E., Heaman, L. M. & Holm, P. M. (1995). Further constraints on the temporal evolution of the Oslo rift from precise U-Pb zircon dating in the Siljan-Skrim area. *Lithos* **34**, 301–315. https://doi.org/10.1016/0024-4937(94)00014-S.

Petersen, J. S. (1978). Structure of the larvikite-lardalite complex, Oslo-region, Norway, and its evolution. *Geologische Rundschau* **67**(1), 330–342. https://doi.org/10.1007/BF01803271.

Pitcher, W. S. (1993). *The Nature and Origin of Granite*. Chapman & Hall, London, https://doi.org/10.1007/978-94-017-3393-9.

Platt, R. G. (1996) Nepheline syenite complexes – an overview. In: Mitchell R. H. (ed) *Undersaturated alkaline rocks: Mineralogy, petrogenesis and economic potential*Mineralogical Association of Canada, Short Course Series 24. Québec: Mineralogical Association of Canada/Association Minéralogique du Canada, pp. 63–99.

Plomerová, J., Arvidsson, R., Babuška, V., Granet, M., Kuhalnek, O., Poupinet, G. & Šileny, J. (2001). An array study of lithospheric structure across the Protogine zone, Värmland, south-Central Sweden – signs of a paleocontinental collision. *Tectonophysics* **332**, 1–21. https://doi.org/10.1016/S0040-1951(00)00247-X.

Raade, G. (1973) *Distribution of radioactive elements in the plutonic rocks of the Oslo region*. Unpublished cand. real. thesis. Norway: University of Oslo.

Rahaman, M. A., Breemen, O., van Bowden & Bennett, J. N. (1984). Age migrations of anorogenic ring complexes in northern Nigeria. *Journal of Geology* **92**, 173–184. https://doi.org/10.1086/628847.

Ramberg, I. B. (1976). Gravimetry interpretation of the Oslo Graben and associated igneous rocks. *Norges Geologiske Undersøkelse* **325**.

Ramberg, I. B. & Larsen, B. T. (1978) Tectonomagmatic evolution. In: Dons J. A. & Larsen B. T. (eds) *The Oslo paleorift. Norges geologiske undersøkelse 337*. Trondheim-Oslo-Bergen-Tromsø: Universitetsforlaget, pp. 105–124.

Rasmussen, E., Neumann, E.-R., Andersen, T., Sundvoll, B., Fjerdingstad, V. & Stabel, A. (1988). Petrogenetic processes associated with silicic magmatism in the Oslo rift, south-East Norway. *Mineralogical Magazine* **52**, 293–307. https://doi.org/10.1180/minmag.1988.052.366.01.

Riishuus, M. S., Peate, D. W., Tegner, C., Wilson, J. R., Brooks, C. K. & Harris, C. (2006). Temporal evolution of a long-lived syenitic Centre: the Kangerlussuaq alkaline complex, East Greenland. *Lithos* **92**, 276–299. https://doi.org/10.1016/j.lithos.2006.03.037.

Riishuus, M. S., Peate, D. W., Tegner, C., Wilson, J. R. & Brooks, C. K. (2008). Petrogenesis of cogenetic silica-oversaturated and –undersaturated syenites by periodic recharge in a crustally contaminated magma chamber: the Kangerlussuaq intrusion, East Greenland. *Journal of Petrology* **49**(3), 493–522. https://doi.org/10.1093/petrology/egm090.

Ro, H. E. & Faleide, J. I. (1992). A stretching model for the Oslo rift. *Tectonophysics* **208**, 19–36. 10.1016/0040-1951(92)90334-3.

Robinson, J. A. C. & Wood, B. J. (1998). The depth of the spinel to garnet transition at the peridotite solidus. *Earth and Planetary Science Letters* **164**, 277–284. https://doi.org/10.1016/S0012-821X(98)00213-1.

de la Roche, H., Leterrier, J., Grandclaude, P. & Marchal, M. (1980). A classification of volcanic and plutonic rocks using R_1R_2-diagram and major element analyses – its relationships with current nomenclature. *Chemical Geology* **29**, 183–210. https://doi.org/10.1016/0009-2541(80)90020-0.

Rosa, D. R. N., Finch, A. A., Andersen, T. & Inverno, C. M. C. (2009). U-Pb geochronology and Hf isotope ratios of magmatic zircons from the Iberian Pyrite Belt. *Mineralogy and Petrology* **95**, 47–69. https://doi.org/10.1007/s00710-008-0022-5.

Salters, V. J. M. & Hart, S. R. (1991). The mantle sources of ocean islands and arc basalts: the Hf isotope connection. *Earth and Planetary Science Letters* **104**, 364–380. https://doi.org/10.1016/0012-821X(91)90216-5.

Schaltegger, U., Schmitt, A. K. & Horstwood, M. S. A. (2015). U-Th-Pb zircon geochronology by ID-TIMS, SIMS, and laser ablation ICP_MS: recipes, interpretations, and opportunities. *Chemical Geology* **402**, 89–110. https://doi.org/10.1016/j.chemgeo.2015.02.028.

Scherer, E. E., Münker, C. & Mezger, K. (2001). Calibration of the lutetium-hafnium clock. *Science* **293**, 683–687. https://doi.org/10.1126/science.1061372.

Scherer, E. E., Münker, C. & Mezger, K. (2007). The Lu-Hf systematics of meteorites: consistent or not. Goldschmidt conference abstracts 2007. *Geochimica et Cosmochimica Acta* **71**, A888.

Schou-Jensen, E. & Neumann, E.-R. (1988). Volcanic rocks on Jeløya, Central Oslo region: the mafic lavas. *Norsk Geologisk Tidsskrift* **68**, 289–308.

Segalstad, T. V. (1979). Petrology of the Skien basaltic rocks, southwestern Oslo region, Norway. *Lithos* **12**, 221–239. https://doi.org/10.1016/0024-4937(79)90006-9.

Sláma, J., Košler, J., Condon, D. J., Crowley, J. L., Gerdes, A., Hanchar, J. M., Horstwood, M. S. A., Morris, G. A., Nasdala, L., Norberg, N., Schaltegger, U., Schoene, B., Tubrett, M. N. & Whitehouse, M. J. (2008). Plešovice zircon - a new natural reference material for U-Pb and Hf isotopic microanalysis. *Chemical Geology* **249**(1–2), 1–35. https://doi.org/10.1016/j.chemgeo.2007.11.005.

Sleep, N. H. (2005). Evolution of the continental lithosphere. *Annual Review of Earth and Planetary Sciences* **33**, 369–393. https://doi.org/10.1146/annurev.earth.33.092203.122643.

Söderlund, U., Patchett, P. J., Vervoort, J. & Isachsen, C. E. (2004). The ^{176}Lu decay constant determined by Lu-Hf and U–Pb isotope systematics of Precambrian mafic intrusions. *Earth and Planetary Science Letters* **219**, 311–324. https://doi.org/10.1016/S0012-821X(04)00012-3.

Sundvoll, B. & Larsen, B. T. (1993). Rb-Sr and Sm-Nd relationships in dyke and sill intrusions in the Oslo rift and related areas. *Norges Geologiske Undersøkelse Bulletin* **425**, 25–41.

Sundvoll, B. & Larsen, B. T. (1994). Architecture and early evolution of the OsloRift. *Tectonophysics* **240**, 173–189. https://doi.org/10.1016/0040-1951(94)90271-2.

Sundvoll, B., Neumann, E.-R., Larsen, B. T. & Tuen, E. (1990). Age relations among Oslo rift magmatic rocks: implications for tectonic and magmatic modeling. *Tectonophysics* **178**, 67–87. https://doi.org/10.1016/0040-1951(90)90460-P.

Sundvoll, B., Larsen, B. T. & Wandaas, B. (1992). Early magmatic phase in the Oslo rift and its related stress regime. *Tectonophysics* **208**, 37–54. https://doi.org/10.1016/0040-1951(92)90335-4.

Swensson, E. (1990). Cataclastic rocks along the Nesodden fault, Oslo region, Norway: a reactivated Precambrian shear zone. *Tectonophysics* **178**, 51–65. https://doi.org/10.1016/0040-1951(90)90459-L.

Thompson, R. N. & Gibson, S. A. (1994). Magmatic expression of lithospheric thinning across continental rifts. *Tectonophysics* **233**, 41–68. https://doi.org/10.1016/0040-1951(94)90219-4.

Trønnes, R. G. & Brandon, A. D. (1992). Mildly peraluminous high-silica granites in a continental rift: the Drammen and Finnemarka batholiths, Oslo rift, Norway. *Contributions to Mineralogy and Petrology* **109**, 275–294. https://doi.org/10.1007/BF00283318.

Turner, D. C. (1963). Ring-structures in the Sara-Fier younger granite complex, northern Nigeria. *Quaterly Journal of the Geological Society of London* **119**, 345–366. https://doi.org/10.1144/gsjgs.119.1.0345.

Turner, D. C. & Bowden, P. (1979). The Ningi-Burra complex, Nigeria: dissected calderas and migrating magmatic centres. *Journal of the Gelogical Society of London* **136**, 105–119. https://doi.org/10.1144/gsjgs.136.1.0105.

Upton, B. G. J. (2020). Tectono-magmatic evolution of the younger Gardar southern rift, South Greenland. *Geological Survey of Denmark and Greenland Bulletin* **29**, 1–124. https://doi.org/10.34194/geusb.v29.4692.

Upton, B. G. J., Emeleus, C. H., Heaman, L. M., Goodenough, K. M. & Finch, A. A. (2003). Magmatism of the mid-Proterozoic Gardar Province, South Greenland: chronology, petrogenesis and geological setting. *Lithos* **68**, 43–65. https://doi.org/10.1016/S0024-4937(03)00030-6.

Valley, J. W., Kinny, P. D., Schulze, D. J. & Spicuzza, M. J. (1998). Zircon megacrysts from kimberlite: oxygen isotope variability among mantle melts. *Contributions to Mineralogy and Petrology* **133**, 1–11. 10.1007/s004100050432.

Villa, I. M., De Bièvre, P., Holden, N. E. & Renne, P. R. (2015). IUPAC-IUGS recommendation on the half life of ^{87}Rb. *Geochimica et Cosmochimica Acta* **164**, 382–385. https://doi.org/10.1016/j.gca.2015.05.025.

Wessel, P. & Husebye, E. S. (1987). The Oslo graben gravity high and taphrogenesis. *Tectonophysics* **142**, 15–26. https://doi.org/10.1016/0040-1951(87)90292-7.

Whitehouse, M. J. & Nemchin, A. A. (2009). High precision, high accuracy measurement of oxygen isotopes in a large lunar zircon by SIMS. *Chemical Geology* **261**, 32–42. https://doi.org/10.1016/j.chemgeo.2008.09.009.

Widenfalk, L. (1972). Myrmekite-like intergrowths in larvikite feldspars. *Lithos* **5**, 255–267. https://doi.org/10.1016/0024-4937(72)90074-6.

Wiedenbeck, M., Allé, P., Corfu, F., Griffin, W. L., Meier, M., Oberli, F., Von Quadt, A., Roddick, J. C. & Spiegel, W. (1995). Three natural zircon standards for U-Th-Pb, Lu-Hf, trace element and REE analyses. *Geostandards Newsletter* **19**, 1–23. https://doi.org/10.1111/j.1751-908X.1995.tb00147.x.

Wiedenbeck, M., Hanchar, J., Peck, W. H., Sylvester, P., Valley, J., Whitehouse, M., Kronz, A., Morishita, Y., Nasdala, L., Fiebig, J., Franchi, I., Girard, J.-P., Greenwood, R. C., Hinton, R., Kita, N., Mason, P. R. D., Norman, M., Ogasawara, M., Piccoli, P. M., Rhede, D., Satoh, H., Schulz-Dobrick, B., Skår, O., Spicuzza, M. J., Terada, K., Tindle, A., Togashi, S., Vennemann, T., Xie, Q. & Zheng, Y.-F. (2004). Further characterization of the 91500 zircon crystal. *Geostandards and Geoanalytical Research* **28**, 9–39. https://doi.org/10.1111/j.1751-908X.2004.tb01041.x.

Wilson, M., Downes, H. & Cebria, J. M. (1995). Contrasting fractionation trends in coexisting continental alkaline magma series; Cantal, massif central, France. *Journal of Petrology* **36**, 1729–1753.

Woodhead, J. D. & Hergt, J. M. (2005). A preliminary appraisal of seven natural zircon reference materials for in situ Hf isotope determination. *Geostandards and Geoanalytical Research* **29**, 183–195. https://doi.org/10.1111/j.1751-908X.2005.tb00891.x.

Woolley, A. R. & Platt, R. G. (1986). The mineralogy of nepheline syenite complexes from the northern part of the Chilwa province, Malawi. *Mineralogical Magazine* **50**, 597–610. https://doi.org/10.1180/minmag.1986.050.358.05.

Workman, R. K. & Hart, S. R. (2005). Major and trace element composition of the depleted MORB mantle (DMM). *Earth and Planetary Science Letters* **231**, 53–72. https://doi.org/10.1016/j.epsl.2004.12.005.

Ziegler, P. A. (1978). *North Sea rift and basin development*. In: Ramberg, I. B. & Neumann, E.-R. (eds.) *Tectonics and Geophysics of Continental Rifts*. D. Reidel Publishing Company, Dordrecht, Holland, pp. 249–277. https://doi.org/10.1007/978-94-009-9806-3_21.

Zindler, A. & Hart, S. (1986). Chemical geodynamics. *Annual Review of Earth and Planetary Sciences* **14**, 493–571. https://doi.org/10.1146/annurev.ea.14.050186.002425.